

Probing the southern African lithosphere with magnetotellurics, Part I, model construction

Max Moorkamp¹, Sinan Özaydin², Kate Selway³, and Alan G. Jones⁴

¹Ludwig Maximilians Universitaet

²Macquarie University

³Future Industries Institute, University of South Australia

⁴Complete MT Solutions

November 26, 2022

Abstract

The Southern African Magnetotelluric Experiment (SAMTEX) involved the collection of data at over 700 sites in Archean to Proterozoic southern Africa, spanning features including the Kalahari Craton, Bushveld Complex and voluminous kimberlites. Here, we present the first 3D inversions of the full SAMTEX dataset. In this paper, we focus on assessing the robustness of the 3D models by comparing two different inversion codes, jif3D and ModEM, and two different subsets of the data, one containing all acceptable data and the other containing a smaller selection of undistorted, high-quality data. Results show that the main conductive and resistive features are imaged by all inversions, including deep resistive features in the central Kaapvaal Craton and southern Congo Craton and a lithospheric-scale conductor beneath the Bushveld Complex. Despite this, differences exist between the jif3D and ModEM inverse models that derive mainly from the differences in regularization between the models, with jif3D producing models that are very smooth laterally and with depth, while ModEM produces models with more discrete conductive and resistive features. Analysis of the differences between these two inversions can provide a good indication of the model resolution. More minor differences are apparent between models run with different subsets of data, with the models containing all acceptable data featuring higher wavelength conductivity variations than those run with fewer stations but also demonstrating poorer data fit.

Abstract

The Southern African Magnetotelluric Experiment (SAMTEX) involved the collection of data at over 700 sites in Archean to Proterozoic southern Africa, spanning features including the Kalahari Craton, Bushveld Complex and voluminous kimberlites. Here, we present the first 3D inversions of the full SAMTEX dataset. In this paper, we focus on assessing the robustness of the 3D models by comparing two different inversion codes, *jif3D* and *ModEM*, and two different subsets of the data, one containing all acceptable data and the other containing a smaller selection of undistorted, high-quality data. Results show that the main conductive and resistive features are imaged by all inversions, including deep resistive features in the central Kaapvaal Craton and southern Congo Craton and a lithospheric-scale conductor beneath the Bushveld Complex. Despite this, differences exist between the *jif3D* and *ModEM* inverse models that derive mainly from the differences in regularization between the models, with *jif3D* producing models that are very smooth laterally and with depth, while *ModEM* produces models with more discrete conductive and resistive features. Analysis of the differences between these two inversions can provide a good indication of the model resolution. More minor differences are apparent between models run with different subsets of data, with the models containing all acceptable data featuring higher wavelength conductivity variations than those run with fewer stations but also demonstrating poorer data fit.

Plain Language Summary

We investigate the structure of the upper 200 km of the Earth beneath southern Africa. To achieve this, we utilize an electromagnetic geophysical technique called magnetotellurics which is sensitive to variations in electrical resistivity within the Earth. To reconstruct electrical resistivity from magnetotelluric measurements, we use so-called inversion algorithms. However, the results are non-unique and a variety of different parameters have to be chosen by the user during the inversion process. In order to better understand the possible variability in our Earth models, we use different inversion algorithms and compare different strategies. This allows us to assess the reliability of our results. Based on our models and their comparison, we infer that the lithosphere, the solid outer shell of the Earth, varies in thickness below our study area and is thickest below central South Africa. In addition, we can detect remnants of past continental col-

49 lisions that have been preserved for hundreds of millions of years since this part of the
50 world was assembled from the collision of various micro-continents.

51 **1 Introduction**

52 The lithosphere of southern Africa is among the most important in the world for
53 understanding continental evolution (e.g., Lee et al., 2011). It contains extensive, Archean
54 to Paleoproterozoic cratons, including the Kaapvaal, Zimbabwe and Congo cratons, which
55 are also sampled by voluminous kimberlite magmatism (e.g., De Wit et al., 1992; Begg
56 et al., 2009). Investigations of the geological, geochemical and geophysical nature of these
57 cratons help us understand the formation and amalgamation of the Archean continen-
58 tal lithosphere and the survival of that lithosphere to the present. The southern African
59 lithosphere also hosts many of the world’s largest mineral deposits (Clifford, 1966), in-
60 cluding the world’s largest platinum group element deposits in the Bushveld Complex
61 (itself the world’s largest layered mafic intrusion (e.g., VanTongeren, 2018)), extensive
62 kimberlite-hosted diamond deposits including the Kimberley, Venetia and Jwaneng de-
63 posits (e.g., Field et al., 2008), and giant orogenic and placer gold deposits such as those
64 in the Barberton Goldfields and Witwatersrand Basin (e.g., de Ronde & de Wit, 1994).
65 Since the formation of many of these deposits involved lithospheric-scale processes, defin-
66 ing the lithospheric architecture and composition of southern Africa not only helps our
67 understanding of continental evolution but also aids mineral exploration.

68 Analysis of the vast mantle xenolith and xenocryst databases has shown spatially
69 and temporally complex patterns of depletion and metasomatism of the southern African
70 mantle (e.g., Griffin et al., 2003; Kobussen et al., 2009; Grégoire et al., 2003). In some
71 cratonic regions, inferences from xenoliths and seismic data can seem contradictory. Many
72 xenoliths have metasomatised and geochemically fertile compositions, while seismic to-
73 mography models tend to show fast wave speeds extending to depths >200 km and have
74 been interpreted to represent deep, geochemically depleted lithospheric keels (e.g., Fouch
75 et al., 2004; White-Gaynor et al., 2020). This apparent contradiction has led to the sug-
76 gession that cratonic mantle xenoliths and xenocrysts from southern Africa may be un-
77 representative of the cratonic mantle more generally (Griffin et al., 2009). In contrast,
78 seismic receiver function data image several low-velocity anomalies within those south-
79 ern African lithospheric keels, which indicate that broad metasomatism may be more widespread
80 than suggested by the tomographic models (Sodoudi et al., 2013; Selway et al., 2015).

81 Here and in the accompanying manuscript, we add new magnetotelluric (MT) con-
82 straints to understanding the architecture, composition and evolution of the southern
83 African lithosphere. MT data are sensitive to mantle metasomatism, both through the
84 hydration of nominally anhydrous mantle minerals and through the precipitation of meta-
85 somatic minerals (e.g., Selway, 2014), and MT interpretations are generally consistent
86 with mantle xenolith and xenocryst compositions (Özaydın et al., 2021). Therefore, MT
87 models of southern Africa can provide new insights into the composition and metaso-
88 matism of the lithosphere. To do this, we have analysed and inverted the Southern African
89 Magnetotelluric Experiment (SAMTEX) database (Jones et al., 2009). These data were
90 collected between 2003–2008 and comprise more than 700 MT stations including broad-
91 band MT (BBMT) and long-period MT (LMT) measurements along more than 15,000
92 line km crossing South Africa, Botswana and Namibia.

93 In this paper, we describe the first 3D MT models of the entire SAMTEX dataset.
94 In contrast to when SAMTEX was collected, 3D MT inversions are now routine. How-
95 ever, different inversion codes use different regularizations, model discretizations and for-
96 ward modelling approaches, and the impact of these differences is not well understood.
97 Therefore, we have inverted the dataset with two different algorithms *jif3D* (Moorkamp
98 et al., 2011) and *ModEM* (Kelbert et al., 2014)) to compare results and ensure only the
99 most robust features are interpreted. In the accompanying paper, we interpret the mod-
100 els in terms of the composition and evolution of the southern African lithospheric man-
101 tle.

102 **2 The SAMTEX magnetotelluric dataset**

103 Magnetotellurics (MT) is a passive electromagnetic technique to infer the resistiv-
104 ity of the subsurface from measurements at the surface (Chave & Jones, 2012). Together
105 with seismic tomography and potential field methods (e.g., gravity, magnetics), MT is
106 one of the foremost geophysical techniques to image the structure of the lithosphere-asthenosphere
107 system. It has been used to investigate continental lithospheric structures in many re-
108 gions around the world (e.g., Jones, 1999; Gatzemeier & Moorkamp, 2005; Rao et al.,
109 2014; Wannamaker et al., 2017; Selway, 2018) and has been a component of large national
110 programs in the United States (Kelbert, 2019), Australia (Kirkby et al., 2020) and China
111 (S.-W. Dong et al., 2013). Based on simultaneous measurements of naturally occurring

112 variations of the electric field \mathbf{E} and the magnetic field \mathbf{B} we can estimate the frequency-
 113 dependent, complex-valued magnetotelluric impedance \mathbf{Z} , viz.

$$\mathbf{E} = \mathbf{Z}\mathbf{B}. \quad (1)$$

114 This estimation process is based on robust statistical methods and thus gives for-
 115 mal estimates of data uncertainties (e.g., Chave & Thomson, 2003) although these are
 116 typically increased before use in an inversion algorithm (e.g., Miensopust, 2017, and dis-
 117 cussion below).

118 The MT response estimates used for our inversions were acquired during the South-
 119 ern African Magnetotelluric Experiment (SAMTEX) between 2003–2008 (Jones et al.,
 120 2009). They comprise more than 700 broadband MT (BBMT) and long-period MT (LMT)
 121 measurements across South Africa, Botswana and Namibia. The primary goal of SAM-
 122 TEX was to image the lithospheric architecture of the cratons and mobile belts in the
 123 region, and thus measurements were taken at intervals of roughly 20 km and at periods
 124 0.01 - 10,000 s for the BBMT sites, and 60 km at 10 s - 10,000 s for the LMT sites. Due
 125 to long recording times and favourable noise conditions in many parts of the study area,
 126 the data quality at many sites is excellent throughout the period range. To date there
 127 have been a number of publications performing modelling and inversions for different sub-
 128 regions and profiles (Hamilton et al., 2006; Muller et al., 2009; Miensopust et al., 2011;
 129 Evans et al., 2011; Khoza et al., 2013; Finn et al., 2015; Moorkamp et al., 2019). In ad-
 130 dition, maps of resistivity directly derived from the data at selected periods have been
 131 used to investigate the structure and composition of the lithosphere-asthenosphere sys-
 132 tem (Jones et al., 2012, 2013) and multi-observable petrological-geophysical models have
 133 been created based on subsets of the data (Fullea et al., 2011). Still, to date, no three-
 134 dimensional resistivity models of the lithosphere based on all the available data have been
 135 published.

136 We show representative data from six stations across the array in Figure 2. Their
 137 locations are shown as yellow stars in Figure 1. We concentrate on the period range of
 138 1–10,000 s as lithospheric-scale structures are the focus of our modelling efforts. The sites
 139 show good data quality throughout the plotted period range, although at the longest pe-
 140 riods ($> 1,000$ s), the scatter and error estimates increase at some of the sites (e.g., KAP45).
 141 The off-diagonal apparent resistivity sounding curves highlight a moderately conductive

142 shallow subsurface ($\approx 10 \Omega\text{m}$ at short periods) at the northern sites RAK011A and ZIM117.
 143 Further south, at sites KIM428 and KAL014, the short period apparent resistivities are
 144 generally comparable but slightly higher, while the southernmost sites, KAP045 and KAP019,
 145 show significantly higher short period apparent resistivities of $\geq 500 \Omega\text{m}$. Beneath this
 146 surface layer, the sounding curves of the four northern sites suggest that resistivity in-
 147 creases with depth to a maximum of $\approx 500 \Omega\text{m}$ at $\approx 500 \text{ s}$, before either remaining con-
 148 stant or decreasing slightly at longer periods. In contrast, at the two southern sites (KAP45
 149 and KAP19), most of the apparent resistivity curves have higher initial values and de-
 150 crease with period.

151 **3 Inversions**

152 **3.1 Inversion Algorithms**

153 We invert the observed MT impedances with two different inversion algorithms (Moorkamp
 154 et al., 2011; Kelbert et al., 2014) and two different strategies for each code. This helps
 155 us to address model uncertainties related to algorithm-specific choices, such as regular-
 156 ization, error floor, model discretization, and precision of the forward modelling engine.
 157 As a result of these choices, each code will fit different aspects of the data, including those
 158 affected by noise, to different degrees. As both algorithms used here are well established,
 159 we only give a brief summary of each algorithm and focus on comparing the differences
 160 and the potential impact on the results.

161 For two inversions, we use the MT inversion module of the joint inversion frame-
 162 work *jif3D* (Moorkamp et al., 2011). The numerical basis of the forward modelling en-
 163 gine and the gradient calculation are presented in Avdeev & Avdeeva (2009) and Avdeeva
 164 et al. (2015). It utilizes an integral-equation based forward engine *x3d* (Avdeev et al.,
 165 1997) and includes a correction for galvanic distortion at each site (Avdeeva et al., 2015;
 166 Moorkamp et al., 2020). Galvanic distortion of magnetotelluric impedances is typically
 167 caused by charge accumulation at small structures (compared to the induction length
 168 scale), and it can mathematically be described as a site-specific, frequency-independent
 169 multiplication of the impedances with a real-valued matrix \mathbf{C} (Chave & Jones, 2012).
 170 In *jif3D* distortion correction is achieved by estimating the elements of \mathbf{C} as part of the
 171 inversion and multiplying the synthetic impedance \mathbf{Z}_{synth} at each site with the corre-

172 sponding distortion matrix when calculating the data misfit. Details on this methodol-
173 ogy can be found in Avdeeva et al. (2015).

174 The inversion algorithm has been used on a range of MT datasets, both commer-
175 cial and academic, including imaging the fault structure for an intra-plate event in Botswana
176 (Moorkamp et al., 2019) and hydrothermal fluids in the central Andes (Pearce et al., 2020).
177 Due to the integral equation based forward modelling algorithm, the horizontal cell sizes
178 need to be constant in both orthogonal horizontal directions. In the vertical direction,
179 cell sizes can vary and are typically fine near the surface, increasing by a constant fac-
180 tor with depth to match the decreasing resolution of MT data. The discretized region
181 is embedded in a layered half-space that is kept constant throughout the inversion. Some
182 care must be taken to avoid the strong influence of this background conductivity struc-
183 ture on the inversion results. In order to enforce positive conductivity values during op-
184 timization and restrict model conductivities to realistic values, conductivities in each model
185 cell are transformed using the generalized model parameter scheme described in Moorkamp
186 et al. (2011). This allows us to use an unconstrained optimization algorithm based on
187 a limited-memory quasi-Newton method (L-BFGS, Avdeeva & Avdeev, 2006) to min-
188 imize the objective function. Within *jif3D* we regularize the inversion through a first-
189 order approximation of the spatial gradient of the generalized model parameters. This
190 approach has the advantage of equalizing the vast range of Earth conductivities ($\approx 10^{-1}$
191 to $10^6 \Omega m$) to a range between approximately -2 and 2, and ensuring that the regular-
192 ization operates similarly in all parts of the model. As the regularization is purely smooth-
193 ness based, it has the potential disadvantage that structures may horizontally or verti-
194 cally smear into regions of low resolution, such as those with poor site coverage in the
195 heterogeneous SAMTEX array. However, this could be considered a form of natural in-
196 terpolation.

197 The other two inversions were performed using *ModEM*, a well-established and freely
198 available 3D MT inversion code (Egbert & Kelbert, 2012; Kelbert et al., 2014). It is widely
199 used in the academic community and has seen applications on datasets around the world
200 (e.g., Kelbert & Egbert, 2012; Meqbel et al., 2014; H. Dong et al., 2020; Robertson et
201 al., 2020). Its forward engine is based on a finite-difference formulation (e.g., Mackie et
202 al., 1994; Egbert & Kelbert, 2012) and its modular structure allows for inversion of dif-
203 ferent combinations of electromagnetic data (e.g., Campanya et al., 2016). Compared
204 to *jif3D* the gridding requirements are less strict with variable-sized rectilinear cells in

205 all three coordinate directions. Furthermore, no background layered half-space is pre-
 206 scribed; instead, the grid must be extensive enough that secondary electromagnetic fields
 207 are insignificant at the model boundaries. Thus, a typical strategy for designing inver-
 208 sion grids in *ModEM* is to use an inner core with constant horizontal cell size and padding
 209 cells of increasing size around it. In *ModEM* the natural logarithm of conductivity is used
 210 as a model parameter which enforces positivity of conductivity and has an equalizing ef-
 211 fect similar to the generalized model parameters in *jif3D*. *ModEM* does not allow the
 212 range of permitted conductivities to be directly limited, but the regularization limits the
 213 difference from a prior model, often the starting model, and lateral variations of conduc-
 214 tivity simultaneously (Egbert & Kelbert, 2012). Compared to a pure smoothing-based
 215 regularization, this combined approach should reduce smearing but can result in arti-
 216 ficial changes in conductivity if the prior model is not representative of the average con-
 217 ductivity in the region. In this case, poorly-resolved regions of the model will be kept
 218 at prior conductivity values, whereas well-resolved regions will exhibit a different con-
 219 ductivity.

220 3.2 Data selection

221 Within each inversion algorithm, we ran an “all data” inversion of the entire SAM-
 222 TEX dataset (with only clearly erroneous stations removed) and another “selected” in-
 223 version of a subset of the data. This approach was designed to test the impacts of het-
 224 erogeneous station coverage and of noisy and distorted data on the results of each in-
 225 version algorithm.

226 SAMTEX station coverage is highly heterogeneous compared to other large-scale
 227 initiatives such as USArray (Kelbert, 2019) or AusLAMP (e.g., Robertson et al., 2016;
 228 Kirkby et al., 2020; Thiel et al., 2020). Due to logistical constraints and the still preva-
 229 lent two-dimensional inversion approaches at the time of planning the measurements, data
 230 were collected in relatively dense transects separated by significant gaps. In a 3D regional
 231 model, the crustal structure will therefore be strongly represented in the data near those
 232 profiles and completely absent in regions without coverage. In contrast, deeper features
 233 (50-200 km) will at least be partially sensed by the data even in regions without direct
 234 station coverage. For this reason, the focus of our inversions will largely be on the re-
 235 gional imaging of the mantle lithosphere-asthenosphere system. To image the mantle,
 236 dense sampling along the profiles could be either beneficial or detrimental. On the one

237 hand, dense coverage should result in redundant information and thus reduce the influ-
 238 ence of noise for deep imaging, but on the other hand, dense measurements can be highly
 239 affected by local structures that cannot be represented well in the regional model. This
 240 issue might be further exacerbated by the need to choose a global regularization param-
 241 eter for the model, as localized structures in densely covered areas might require a small
 242 regularization parameter. However, small regularization parameters might be inappro-
 243 priate for regions without dense coverage.

244 The noise levels of SAMTEX data are also heterogeneous (Figure 3). Some sites
 245 show significant noise across the whole period range, with either highly scattered or phys-
 246 ically unrealistic data (e.g., ELG010A). These sites were excluded from all inversions.
 247 Of the remaining sites, some (e.g., BOT405) display smooth sounding curves with phases
 248 in quadrant but also demonstrate large offsets between the apparent resistivity curves,
 249 indicating local static distortion. Others (e.g., KAP047 and WIN011) show similar signs
 250 of static distortion and additionally display rapidly varying phases that extend out of
 251 the quadrant, which could indicate local noise or strong resistivity contrasts in the shal-
 252 low subsurface. Even though *jif3D* can correct for distortion and strategies have been
 253 devised for *ModEM* to mimic the effects of distortion (Meqbel et al., 2014), it is unclear
 254 to what degree the information from these sites is useful to constrain deep structures and
 255 whether fitting distorted sites prevents fitting other data. To investigate the impact of
 256 such sites, they were therefore retained in the “all data” inversion but excluded from the
 257 “selected” inversion. To further reduce station density and to assess the impact of het-
 258 erogeneous station coverage, additional stations with low-quality long-period data (> 500 –
 259 10000 s) were also removed. After the selection procedure, the resulting “selected” dataset
 260 has a station spacing along the station transects of ~ 30 – 80 km in most regions, com-
 261 pared to ~ 20 km for the “all data” dataset (compare blue and red dots in Figure 1).

262 **3.3 Inversion Setup**

263 To be able to accommodate the entire region in a single model with acceptable com-
 264 putational run times, the horizontal discretization for the core region was chosen to be
 265 15 km in the northing and easting directions for all inversions. Including the padding
 266 cells for the runs with *ModEM*, the inversion domain comprises $132 \times 133 \times 53$ cells with
 267 a vertical discretization of 50 m for the topmost cells increasing up 141 km at the bot-
 268 tom of the domain. Information on ocean bathymetry was introduced from the ETOPO1

269 global topographic dataset, and seawater was assigned a resistivity of $0.3 \Omega m$. On land,
 270 no topography was considered, and a starting resistivity of $100 \Omega m$ was assigned to all
 271 cells.

272 Inversions for *ModEM* were run with error floors of 5% of $\sqrt{Z_{xy}Z_{yx}}$ on all tensor
 273 elements. The starting λ was set to 10 and decreased by a factor of 5 when the inver-
 274 sion when RMS misfit difference is less than 0.002. An isotropic smoothing operator was
 275 constructed with the covariance matrix set to 0.4 in all directions. For the inversions with
 276 *jif3D*, we used the same error floor as for the inversions with *ModEM*. We removed the
 277 outer padding cells from the grid used for modelling in *ModEM* resulting in a mesh with
 278 $119 \times 120 \times 48$ cells and chose a fixed background resistivity of $100 \Omega m$.

279 The inversions for *jif3D* were run with a similar approach to regularization as the
 280 inversions with *ModEM*. However we used different values for the regularization param-
 281 eter, starting with $\lambda = 1,000$ and reducing it to $\lambda = 1$ in the final iterations, since the
 282 influence of the regularization on the inversion is different between the two algorithms.
 283 The initial iterations did not include any distortion correction, but this was enabled af-
 284 ter the first regularization change as this has been shown to yield stable results (Moorkamp
 285 et al., 2020).

286 4 Data fit

287 For the selected datasets the inversion algorithms reach a final RMS of 1.7 (*jif3D*)
 288 and 2.3 (*ModEM*) after 200 and 146 inversion iterations, respectively. For the inversion
 289 of the full datasets, the corresponding RMS values are 2.7 and 5.0, respectively. We show
 290 the final root-mean-square (RMS) misfit at each site for all frequencies in Figure 5. When
 291 we only invert the selected data (bottom row) using both *jif3D* and *ModEM* we achieve
 292 a relatively homogeneous RMS between 1.5 and 2.5 at the majority of sites, and only
 293 a few sites exceed RMS values of 4.5. While there are some differences in how well sites
 294 are fit, the overall pattern is comparable and some sites are fit better in one inversion
 295 or the other. In contrast, when inverting the maximum amount of data, the distribution
 296 of RMS becomes much more heterogeneous. Many sites are still in the 1.5 to 2.5 range,
 297 but some sites exceed RMS values of 10. This effect appears to be more pronounced for
 298 *ModEM* than *jif3D* and some sites that were fit well in the “selected” inversion are now
 299 fitted significantly worse. These observations confirm that some data that were excluded

300 are, in fact, problematic for the inversion. At least for some of these sites, the distortion
 301 correction used by *jif3D* helps to achieve a better fit. The question remains, though, to
 302 which degree this impacts the final models.

303 Figure 4 shows the estimated values of the distortion matrix \mathbf{C} for the two *jif3D*
 304 inversions at the central area of the array around the sites BOT405 and KAP047 (Fig-
 305 ure 3) that were previously identified as distorted (a version with all stations can be found
 306 in the supplementary material). For the selected data inversion, \mathbf{C} is close to the iden-
 307 tity matrix at virtually all sites indicating little to no galvanic distortion. This demon-
 308 strates that the data selection process successfully removed stations with significant dis-
 309 tortion and that the inversion algorithm does not introduce artificial distortion, for ex-
 310 ample, to achieve a low data misfit with a smooth model. When inverting the complete
 311 data set, some but not all of the additional sites show significant distortion and sites BOT405
 312 and KAP047 are among the most distorted (Figure 4).

313 In theory, if galvanic distortion is caused by structures that are small compared to
 314 the typical induction scale length at short periods (Chave & Jones, 2012) and the dis-
 315 tortion correction only represents this structure-related distortion, the estimates of \mathbf{C}
 316 at neighbouring sites should show little correlation. Although this is the case in some
 317 regions, we also see clusters of sites with very similar distortion estimates, e.g., south of
 318 site BOT405. Here the estimate of C_{xx} is consistently larger than unity and C_{yy} smaller
 319 than unity at most sites. There are two possible explanations for this phenomenon: a)
 320 It is possible that these sites were all installed in similar geological conditions, for ex-
 321 ample, when looking for softer ground in an environment dominated by outcropping bedrock.
 322 b) More likely, the distortion estimates capture variability in structures that can, in prin-
 323 ciple, be resolved by MT measurements but cannot be represented by the chosen hor-
 324 izontal discretization of 15 km, i.e. they account for the so-called model discrepancy (Kennedy
 325 & O’Hagan, 2001). These stations are located at the northern end of the Kaapvaal Cra-
 326 ton crossing into the Magondi Mobile Belt, and thus it is likely that significant defor-
 327 mation is recorded in the crust.

328 We compare the data fit for the distorted site BOT405 and and the exemplary sites
 329 RAK011A, KIM428 and KAP045 for the *ModEM* “all data” inversion (Figure 6) and
 330 the *jif3D* “all data” inversion (Figure 7). The difference between observed and predicted
 331 data for site BOT405 clearly shows how the distortion correction in *jif3D* helps to achieve

332 a better fit to the off-diagonal apparent resistivity curves. Whereas the model response
 333 from *ModEM* converges to a common apparent resistivity value at short periods, *jif3D*
 334 reproduces the constant offset between the two curves. Interestingly, although the off-
 335 diagonal phases are fit differently by both inversions, there is no clearly superior fit by
 336 either of the two models. At sites RAK011A and KIM428, both models produce virtu-
 337 ally identical responses for the off-diagonal apparent resistivities and phases and match
 338 the observed data well. At site KIM428, the models reproduce all variations of the curves,
 339 while at site RAK011A, the overall shape is reproduced well by the models, but the phase
 340 anomaly in the xy-component at periods between 50-100 s is not fully reproduced by ei-
 341 ther model. At both stations, the diagonal elements are significantly smaller than the
 342 off-diagonal elements and are matched better by the *jif3D* inversion than the *ModEM*
 343 inversion. It is our experience that distortion correction helps to match diagonal elements
 344 better even when these are small (Moorkamp et al., 2020). The data at site KAP045 are
 345 matched differently by the two inversions, and again the difference is more pronounced
 346 in the phase than in apparent resistivity. The response from *ModEM* reproduces the short
 347 period phases well but shows small but consistent differences in the overall shape. In com-
 348 parison, *jif3D* appears to reproduce aspects of the general shape better but does match
 349 the phases exactly in any period range.

350 The observed differences in model fit highlight that different inversion algorithms
 351 reproduce different aspects of the observed data that go beyond the changes expected
 352 from simply modifying the regularization in a single inversion algorithm. This contrast-
 353 ing behaviour illustrates the value of inverting data with multiple inversion algorithms.
 354 It also shows that distortion correction can help fit certain aspects of the data, as demon-
 355 strated by the misfit maps, but this does not necessarily imply that all aspects of the
 356 data are matched more closely. All in all both inversions with all data match the obser-
 357 vations at the majority of sites well. We therefore expect both models to provide rea-
 358 sonable representations of electrical resistivity in the vicinity of the measurements sites.

359 5 Resistivity models

360 We show horizontal cross-sections through the derived inversion models between
 361 50 and 200 km depth in 50 km intervals (Figures 8 - 11) as well as vertical slices in the
 362 east-west direction at latitude 22° south (Figure 12) and along the Kaapvaal (Figure 13)
 363 and Kimberley (Figure 14) profiles (see also Figure 1 for location of these profiles). The

364 different inversions show very similar large-scale structures, e.g., a generally resistive (\geq
 365 $500 \Omega m$) central region below 50 km depth, which is significantly more resistive than the
 366 starting model ($100 \Omega m$). Embedded in this resistive lithosphere are several large con-
 367 ductors, typically associated with boundaries of different geological units. Even though
 368 the large-scale picture is similar for all models, there are significant differences in the de-
 369 tailed resistivity structures and values between the inversion results. We will therefore
 370 start with a description of the main features based on the “all data” *jif3D* model and
 371 discuss how these are expressed in the other models. In the next section, we use the dif-
 372 ferences and similarities between the models to appraise the robustness and resolution
 373 of inversion results.

374 We observe the maximum resistivity ($\geq 5,000 \Omega m$) around the south-eastern part
 375 of the array (labelled the Kaapvaal Resistor (KR) on the horizontal slices) and the north-
 376 western part of the array, north of the Damara Conductive Belt (DCB). In both cases,
 377 the maximum resistivity is located at depths between 50–100 km and appears to decrease
 378 at 150 km depth and below. These observations are compatible with the thick, dry litho-
 379 spheric mantle associated with the roots of the Kaapvaal Craton and the Congo Cra-
 380 ton, respectively (e.g., Evans et al., 2011; Jones et al., 2013; Khoza et al., 2013). In the
 381 central part of the array, around latitude 24° south, is a roughly east-west striking band
 382 of reduced resistivity ($\sim 100 \Omega m$) in the deeper slices (150 km and below) which becomes
 383 more resistive in the shallower parts of the model. We term the central structure in this
 384 band at approximately 24° east the Molopo Farms Conductor (MFC). It can be iden-
 385 tified as a zone of decreased resistivity ($< 20 \Omega m$) on the 150 km and 200 km depth slices
 386 from the two *ModEM* inversions. The *jif3D* based inversions only show a weak signa-
 387 ture at 150 km but show a structure with similarly low resistivity displaced slightly to
 388 the north-west at 200 km depth. The conductor associated with Bushveld Complex (Bushveld
 389 Conductor, BC) appears on all different modelling schemes north of the Kaapvaal Re-
 390 sistor (KR, Figure 13). Even though its conductivity differs from model to model, less
 391 than $10 \Omega m$ in the inversions with *ModEM* and $30\text{--}50 \Omega m$ in the inversions with *jif3D*
 392 , its spatial extent is consistent between models and it is consistently positioned beneath
 393 the surface expression of the Bushveld intrusive complex, suggesting that it is a robustly
 394 modelled feature.

395 Further south, the *ModEM* inversions indicate a low resistivity zone ($20 \Omega m$) at
 396 a depth of 50 km near the south-western terminus of the Kaapvaal Craton, which we term

397 the Southern Kaapvaal Conductor (SKC). The “selected data” *ModEM* inversion shows
398 this low resistivity extending to depths ≥ 150 km, but this is less clearly visible in the
399 inversion with all data. Both *jif3D* inversions show decreased resistivities of $100 \Omega \text{ m}$ com-
400 pared to the surrounding $1,000 \Omega \text{ m}$, but no structures with the low resistivity indicated
401 by *ModEM*.

402 In the north-western part of the array, the signature of the Damara Conductive Belt
403 (DCB), previously identified by Khoza et al. (2013), is apparent at a depth of 50 km in
404 all inversions. It is an east-west striking band of decreased resistivity ($\sim 10 \Omega \text{ m}$), inter-
405 preted to be associated with the collision between the Congo Craton and the adjacent
406 mobile belts. At depths of more than 100 km, the inversions with all data also contain
407 an approximately north-south striking, low resistivity feature. The inversions with se-
408 lected data also show slightly decreased resistivity in the same region, but it appears that
409 some information on this feature is contained in the sites excluded in the selection pro-
410 cess.

411 In addition to these four features discussed above, the model contains a variety of
412 other structures. We do not go into further detail on all these features here but in the
413 second part of this study (Özaydin et al., 2021) we investigate the relationships between
414 the geoelectric lithospheric architecture, composition, tectonic and magmatic history of
415 the southern Africa in detail.

416 The vertical slices through the model shown in Figures 12 - 14 confirm the infer-
417 ences made by comparing the horizontal slices, showing similar low and high resistivity
418 features. However, the exact locations, shapes and resistivity values vary between the
419 different inversions. In all cases, the “all data” inversions show stronger resistivity con-
420 trasts and more localized features than the “selected data” inversions for the same in-
421 version algorithm, particularly in the upper 50 km. Below this depth, the differences be-
422 tween using all data and selected data are less pronounced, but persist. For example, the
423 *ModEM* “all data” slice along the KAP line (Figure 13) shows a low resistivity zone at
424 a depth of 200 km towards the northern (right) end of the profile. This feature is not
425 clear in the “selected data” inversion, which shows resistivity values comparable with
426 the starting model, possibly suggesting that there is little resolution in this region. Com-
427 paring the results from the two different inversion algorithms, *ModEM* appears to favour

428 more concentrated features at depth while in *jif3D* the features are generally more dis-
 429 tributed with less sharp edges.

430 6 Model appraisal

431 To provide a quantitative view on the differences between the models, we plot model
 432 difference matrices at a depth of 50 km in Figure 15 and 150 km in Figure 16. In both
 433 cases, we show a horizontal slice through each model at the respective depth on the di-
 434 agonal. Plots above the diagonal show the difference in logarithmic resistivity for the dif-
 435 ferent model combinations, while plots below the diagonal show the corresponding re-
 436 sistivity difference histograms. The model histograms show significant differences in re-
 437 sistivity between all model combinations of up to 2 orders of magnitude (2 in logarith-
 438 mic units), even though for the vast majority of model cells, the difference is less than
 439 ± 1 order of magnitude. The histograms appear to be slightly wider at 50 km depth than
 440 at 150 km depth. Most histograms are centered around a difference of zero, suggesting
 441 that there is no significant overall bias in the resistivities retrieved in each inversion, ex-
 442 cept the histogram for the two inversions with selected data, which is centered around
 443 ≈ 0.2 , indicating that the model produced by *jif3D* is consistently more resistive.

444 The histograms clearly illustrate that the largest resistivity differences are produced
 445 by using different algorithms to invert the same dataset, while smaller differences are pro-
 446 duced by inverting different subsets of data with the same inversion algorithm. At both
 447 depths and for both inversion algorithms, the histograms comparing the “selected” and
 448 “all data” inversions show highly symmetric shapes and a concentrated peak at zero, while
 449 the other histograms are generally broader and exhibit more structure.

450 The spatial difference plots in Figures 15 and 16 add more detail to the global re-
 451 sistivity differences displayed in the histograms. Spatial comparisons between the *jif3D*
 452 and *ModEM* models using both “selected data” and “all data” datasets at both depths
 453 consistently show that the *jif3D* models have higher average resistivities over much of
 454 the model space than the *ModEM* models, except for in the south-western part of the
 455 array where *jif3D* produces a consistently less resistive model. The south-western region
 456 is the part of the model most poorly constrained by station coverage. These differences
 457 sum to a resistivity difference histogram that centers on zero. In all difference plots, we
 458 also see a correlation between locations of large scale tectonic boundaries and changes

459 in sign of the resistivity difference, particularly along the northern margin of the Namaqua-
460 Natal Belt and the margins of the Damara and Ghanzi-Chobe belts. While the details
461 vary, this phenomenon is observed in all combinations of models to varying degrees. This
462 indicates that the differences in the models are not merely due to fitting aspects of the
463 data differently or the influence of noisy measurements, but each inversion images the
464 Earth in a different way.

465 Comparisons between the two “selected data” inversions and the two “all data” in-
466 versions demonstrate that data selection has a significant impact on model differences.
467 The spatial difference plots for the *jif3D* and *ModEM* “selected data” inversions reveal
468 broad zones of consistent resistivity differences, while those for the two “all data” inver-
469 sions show much more inhomogeneous, spatially varying resistivity differences. This re-
470 sults from the stronger influence of regularization in the “selected data” inversions, lead-
471 ing to overall smoother models. When adding data, the wavelength of the patterns de-
472 creases, and we see more fine-scaled differences, together with relatively sharp changes
473 between positive and negative differences. Some of the largest differences are located in
474 regions without site coverage, e.g., southeast of the KAP line or in the gaps between mea-
475 surement lines in the northern part of the array.

476 The most likely candidate for causing many of these differences is the different reg-
477 ularization schemes. This factor is most clearly seen in the comparison between mod-
478 els produced with the “selected” dataset as the influence of regularization is strongest
479 there. Where the Earth is more resistive than the starting model in both inversions, *jif3D*
480 consistently estimates higher resistivities than *ModEM*. Conversely, where the inversions
481 indicate lower resistivities than the starting model, *jif3D* underestimates resistivity com-
482 pared to *ModEM* on the larger scale. Both observations can be explained by the fact that
483 *ModEM* minimizes the difference to the reference model and smoothness simultaneously,
484 while *jif3D* only aims at recovering a smooth model. This behaviour can explain the ob-
485 served correlation between major tectonic boundaries and changes in sign of the resis-
486 tivity difference. A resistive geological region is likely to be modelled with a higher re-
487 sistivity in *jif3D* than *ModEM*, and an adjacent conductive geological region is likely to
488 be modelled with a lower resistivity in *jif3D* than *ModEM*. The model difference plot there-
489 fore highlights the boundary between these two regions.

490 Without additional information, we cannot say which of the inversions is more rep-
491 resentative of the true resistivity within the Earth. However, we tried to reduce the ef-
492 fect of regularization in *ModEM* by running an additional inversion with a starting and
493 reference model based on laterally smoothed apparent resistivities. To construct this model,
494 for each measurement site we construct a circle with a 4-degree radius centred on the
495 site and take the median apparent resistivity value of all sites within the circle at peri-
496 ods longer than 100 s. The resulting resistivity value is assigned to all cells below this
497 site. We then perform a linear interpolation of logarithmic resistivity between these val-
498 ues to determine the resistivity in each model cell. The resulting model (Figure 17) shows
499 laterally varying resistivities between 50 and 1,000 Ωm and regions of high resistivity that
500 correlate with the most resistive regions identified in the previous inversions.

501 The resulting median inversion model (Figures 18 and 19) fits the selected data to
502 an RMS comparable with the inversion run from a homogeneous half-space. Compared
503 to the homogeneous inversion run, the average resistivities at 50 km depth (Figure 18)
504 and 150 km depth (Figure 19) are higher, particularly in regions that are not directly
505 covered by sites. Conductive anomalies show a very similar pattern to the previous in-
506 versions, although the shape and location differ slightly in some cases, including some
507 of the individual conductors that form the Damara Conductive Belt at 50 km depth (com-
508 pare Figure 8 and Figure 18) or the Southern Kaapvaal Conductor at 150 km depth. These
509 changes are not significant enough to imply a different geological interpretation of these
510 structures.

511 The spatial difference plot and difference histogram comparing the median inver-
512 sion and the inversion of the same data with *jif3D* reveals some interesting changes com-
513 pared to the inversion with a homogeneous starting model. Visually, the spatial differ-
514 ence plot for the median model contains a lot less long-wavelength structure and is dom-
515 inated by more small scale differences. This contrast is particularly visible at 50 km depth
516 where *jif3D* previously produced consistently higher resistivities in the central model re-
517 gion. However, the spatial difference plot for the median model displays a much more
518 variable pattern where the sign of the conductivity difference changes within smaller dis-
519 tances. At 150 km depth, the effect is less pronounced yet still observable.

520 The difference histogram comparing the median inversion and the *jif3D* inversion
521 at 50 km depth has a maximum very close to zero, while the histogram comparing the

522 homogeneous inversion and *jif3D* is offset to slightly positive values with a maximum
 523 at ≈ 0.2 . While still not fully symmetric, the maximum and minimum (most negative)
 524 differences now show a similar magnitude. At 150 km depth, the impact of the starting
 525 model on the histogram is even more pronounced and the median model histogram is
 526 more significantly offset to negative values associated with the higher average resistiv-
 527 ity of the median model. While the average resistivities inverted from the homogeneous
 528 *ModEM* are downward biased compared to *jif3D*, the median model *ModEM* resistiv-
 529 ities are upward biased.

530 7 Discussion and Conclusions

531 The main goal of this paper is to present a new 3D conductivity model for south-
 532 ern Africa and use the different inversion methodologies to understand uncertainties in
 533 the results better. An additional result is that the detailed comparisons of the models
 534 also reveal some technical aspects of inversions and regularization that are of interest to
 535 both algorithm developers and practitioners and thus warrant some discussion before de-
 536 scribing some of the geological interpretations implied by these models.

537 It is our impression that most of the differences between the results from the two
 538 inversion algorithms stem from the different regularization philosophies. The purely smooth-
 539 ness based approach followed by *jif3D* spreads out structures to their maximum possi-
 540 ble extent, most clearly visible in Figure 13. Selecting such a smoothing operator has
 541 the disadvantage that conductive anomalies can be smeared out, and their boundaries
 542 can be challenging to identify. In contrast, the mixed regularization approach pursued
 543 by *ModEM* typically produces more localized structures. On the flip side, the regular-
 544 ization toward a reference model appears to bias the large scale resistivity toward this
 545 model, particularly in regions of low sensitivity. This observation is mirrored by the sys-
 546 tematic study of Robertson et al. (2020). Taken together, we conclude that for large ar-
 547 rays with heterogeneous coverage such as this, *jif3D* produces models with more repre-
 548 sentative large-scale resistivity values, while *ModEM* produces more focused and local-
 549 ized anomalies. To some degree, a more representative large-scale resistivity can be ob-
 550 tained with *ModEM* with a median-based starting model, as shown by the comparison
 551 at 50 km depth. Still, the shift in bias at 150 km shows that possibly a more detailed
 552 starting model with varying resistivity with depth is necessary to obtain good average
 553 resistivities over large areas. Alternatively, one could design a regularization scheme where

554 the balance between smoothness and damping toward a reference model can be finely
 555 adjusted. While it seems that such an approach could combine the advantages of both
 556 regularization approaches, it is questionable how an optimal balance could be objectively
 557 found and how practical such a scheme would be for routine application.

558 The effect of inverting for only selected, high-quality data or the maximum amount
 559 of data is similar regardless of the inversion algorithm. In both cases, the inclusion of
 560 more data increases the misfit of the final models as potentially problematic sites are in-
 561 troduced. To some degree, this effect is reduced by the distortion correction employed
 562 in *jif3D* which can deal with problems associated with galvanic distortion and achieve
 563 a better fit at many sites. At the same time, the models with more data exhibit stronger
 564 resistivity contrasts and additional structures, e.g., the north-south striking conductor
 565 in the north-western part of the study area that extends from the Congo Craton into the
 566 Damara Belt. Given the similarity of these features for both inversion algorithms and
 567 the acceptable misfit for the inversion with *jif3D*, we conclude that these are not arte-
 568 facts caused by noisy data, but that these features are due to information about the re-
 569 sistivity of the Earth contained in the measurements included in the “all data” models.
 570 Still, the inversions with selected data contain the same general features as the inver-
 571 sions with all data. Based on the similarity with other models and the data fit, our two
 572 preferred models are the ones produced by *jif3D* with all data and the *ModEM* inver-
 573 sion with a median starting/reference model and selected data.

574 The most prominent features of our two preferred models are: (1) A resistive core
 575 of the Kaapvaal Craton as indicated by the Kaapvaal Resistor. This region of high re-
 576 sistivity ($> 1,000\Omega m$) extends to depths of 150 km (*ModEM*) to 200 km (*jif3D*) and
 577 indicates a dry lithospheric mantle in line with previous 2D interpretations (Evans et al.,
 578 2011) and experimental electrical conductivity of common mantle minerals (e.g., Karato
 579 & Wang, 2012; Özaydın & Selway, 2020). (2) Other high resistivity regions at depths of
 580 100 km and greater include the Congo Craton in the north-west (Kamanjab Inlier) and
 581 northern Botswana in the north-eastern part of the array suggesting the presence of litho-
 582 sphere with a broadly similar composition in these regions. (3) These resistors are in-
 583 tersected by several deep-seated conductors that are present to varying extents in all in-
 584 version models. These include the Molopo Farms conductor, the Bushveld conductor and
 585 the north-south striking feature below the Congo Craton and Damara Belt. In the lat-
 586 ter case, a possible interpretation is a shallower lithosphere-asthenosphere boundary com-

587 pared to the thick cratonic roots of the Kaapvaal and Congo Cratons (Celli et al., 2020).
588 In contrast, the Molopo Farms Conductor and the Bushveld Conductor are likely expres-
589 sions of emplacement of metasomatic material during episodes of magmatism (Beukes
590 et al., 2019).

591 A more detailed interpretation of the resistivity structures recovered by these in-
592 versions requires careful consideration of the geological history of the region and the re-
593 lationships between resistivity, composition and temperature. These considerations are
594 beyond the scope of this study and are presented in a companion paper (Özaydin et al.,
595 2021).

596 We have constructed a set of 3D models for southern Africa based on two subsets
597 of the SAMTEX magnetotelluric dataset and utilizing two independent inversion algo-
598 rithms. Despite some differences in the shape of structures and the recovered resistiv-
599 ities, the models show strong similarities. Previous efforts using these data either used
600 the whole dataset but did not perform inversions or were concentrated on regional sub-
601 sets of the data. Thus the models presented here are the first large-scale resistivity mod-
602 els of the region and can serve as a resource for further investigations and integration
603 with other observations such as gravity and seismology.

604 **Acronyms**

605 **BBMT** Broad-Band Magnetotelluric

606 **BC** Bushveld Conductor

607 **DCB** Damara Conductive Belt

608 **MT** Magnetotelluric

609 **KR** Kaapvaal Resistor

610 **LMT** Long-period Magnetotelluric

611 **MFC** Molopo Farms Conductor

612 **SAMTEX** South African Magnetotelluric Experiment

613 **SKC** Southern Kaapvaal Conductor

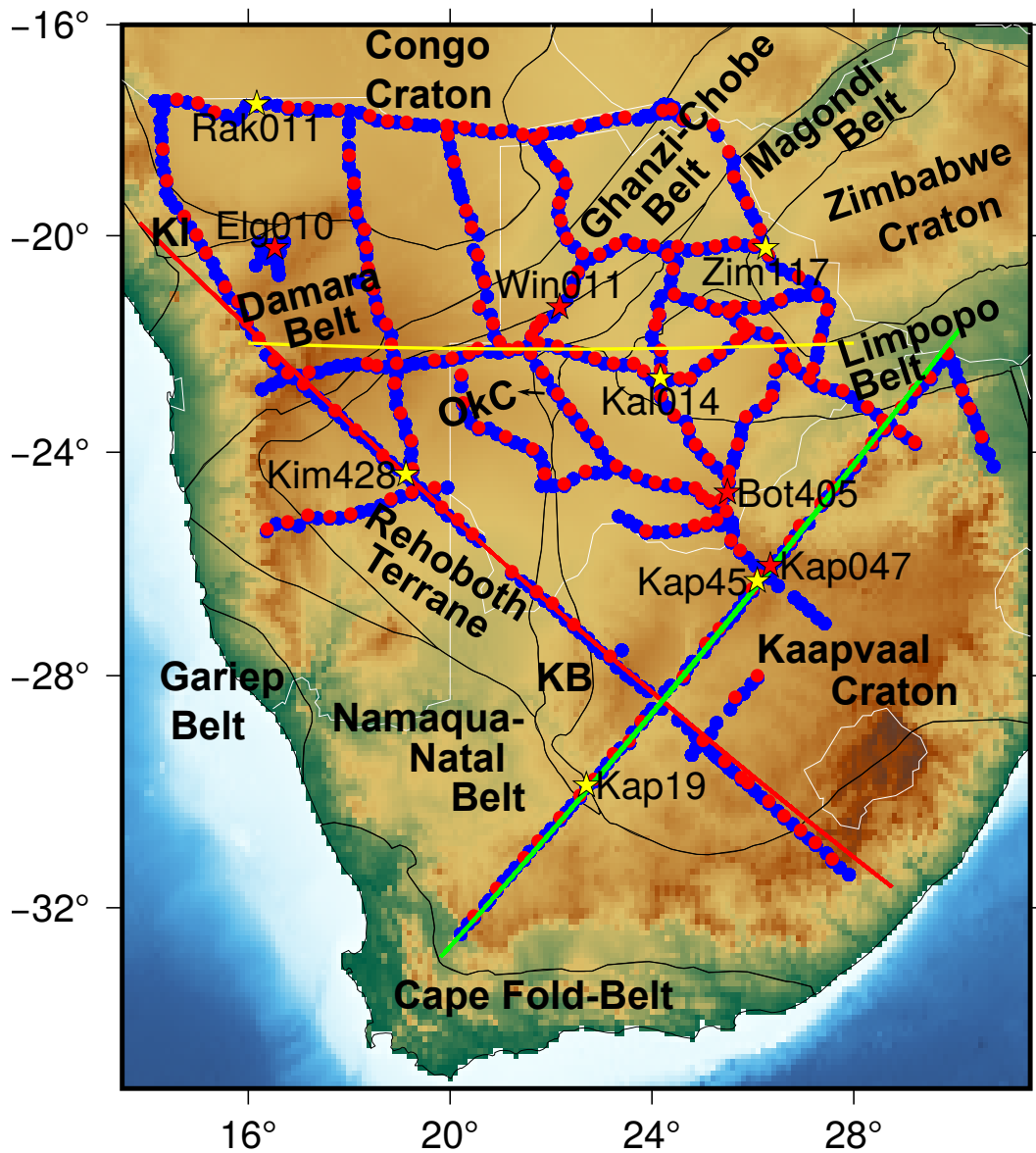


Figure 1. Map of the study area. We show the SAMTEX magnetotelluric measurement sites considered in the full data inversions as blue dots and the sites considered in the inversions with selected data as red dots. Yellow stars indicate exemplary stations for different regions shown in Figure 2 and red stars poor quality data excluded from some of the inversions and shown in Figure 3. The red, green and yellow lines mark the locations of vertical model profiles along the Kimberley, Kaapvaal and 22 degree south lines, respectively. Black lines mark the boundaries of tectonic provinces based on McCourt et al. (2013).

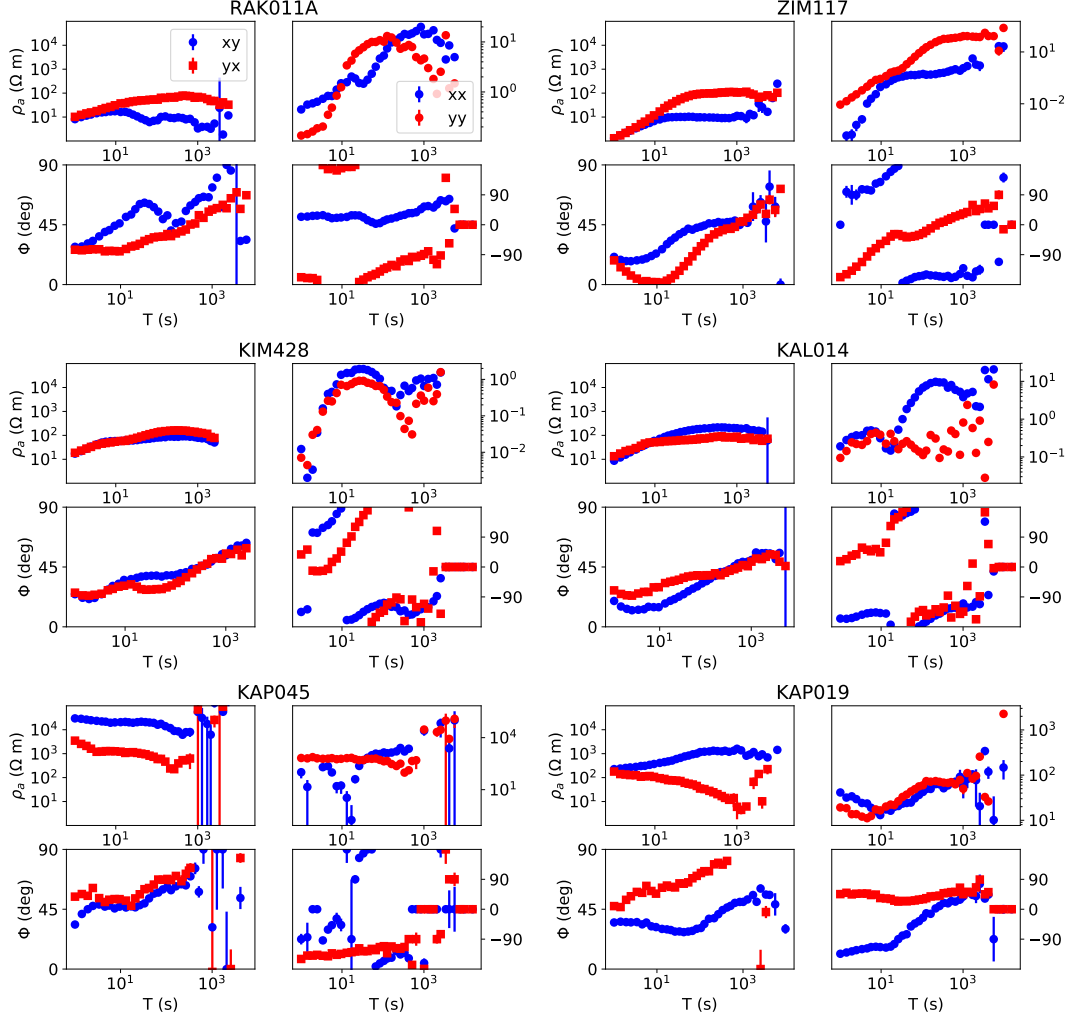


Figure 2. Six exemplary sites representing different regions within the inversion domain. For each site we plot apparent resistivity and phase of the four impedance elements. Off-diagonal (xy and yx) apparent resistivities are plotted with a consistent y-axis to highlight differences in average resistivity between different regions, while apparent resistivity for the diagonal components is plotted with a different scale for each site for better readability.

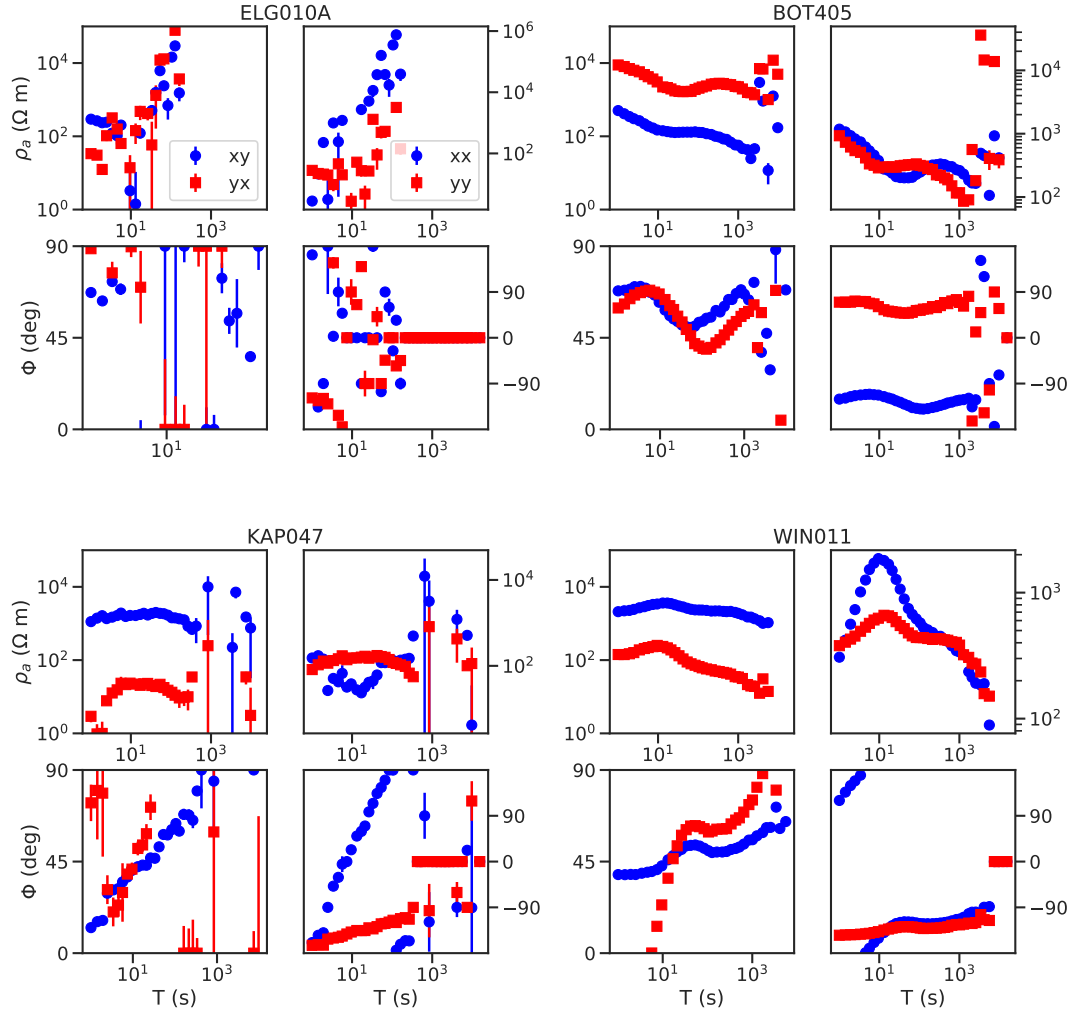


Figure 3. Examples of data excluded from the inversions with selected data. Site ELG10A shows overall problematic data and has been excluded from all inversions while the other sites show potentially problematic features as discussed in the text but have been retained for the inversions with maximum data.

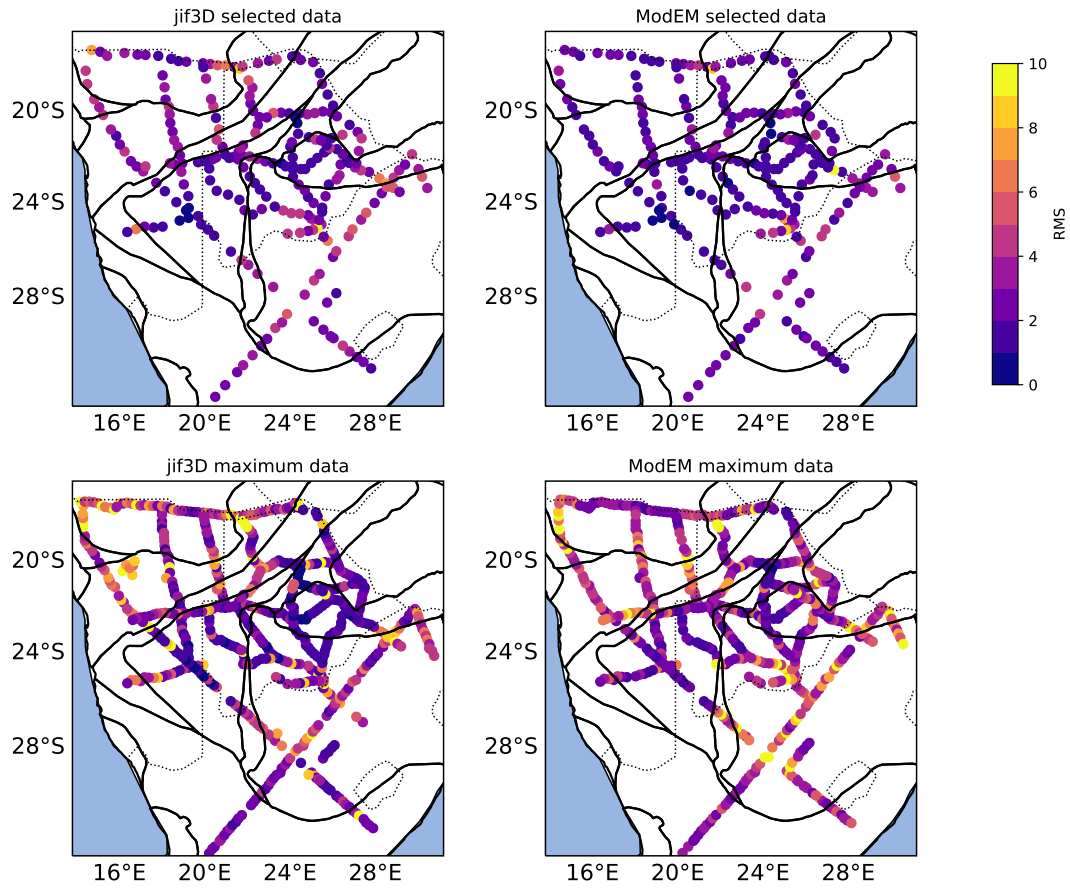


Figure 4. Map of misfit for the four inversion runs. We show the error normalized RMS across all frequencies at each site.

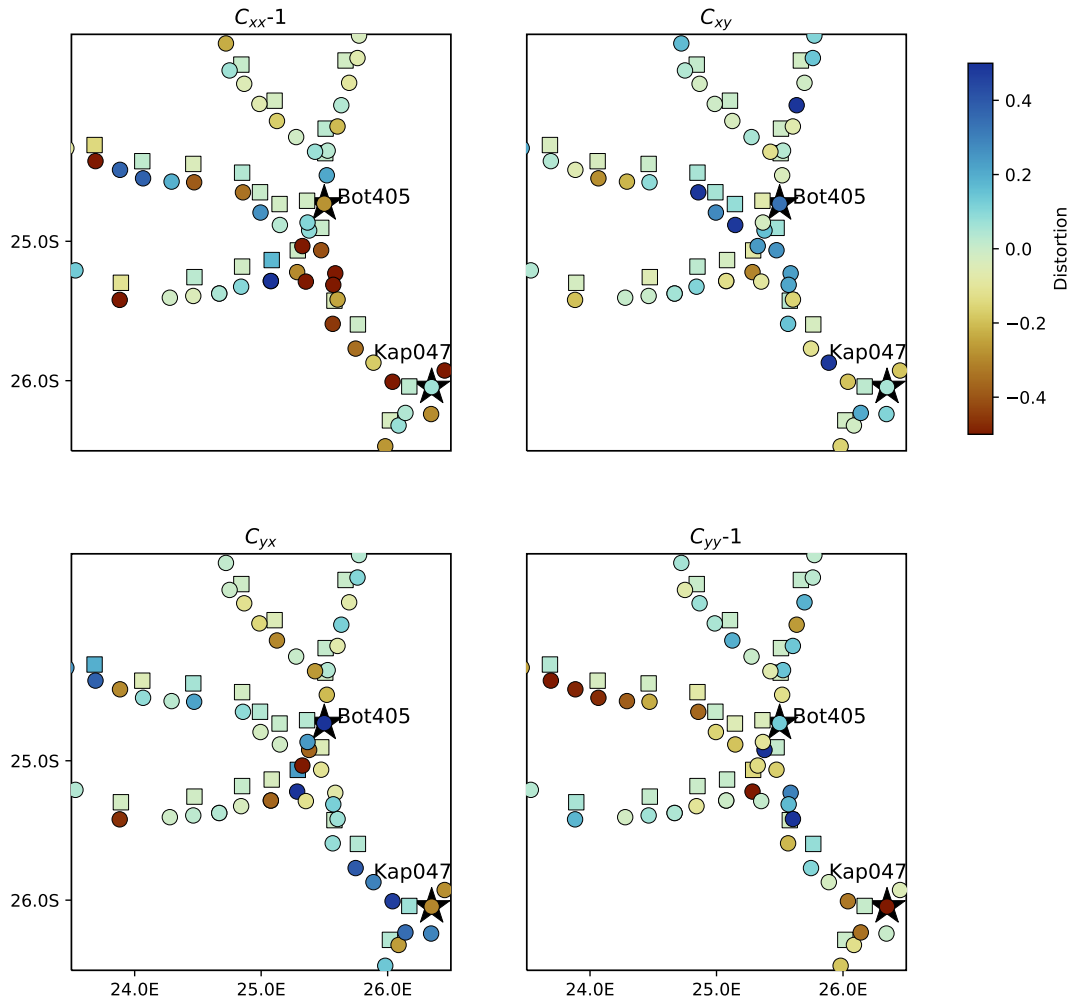


Figure 5. Map of distortion estimates for the inversions with *jif3D* in the central region of the array. We show the estimates for the inversion with all data as circles and for the selected data inversion as squares. These have been displaced north from the original locations for better visibility. Colors mark the deviation of the distortion matrix elements from the identity matrix. We highlight sites BOT405 and KAP047 shown in Figure 3 with black stars.

Data fit ModEM

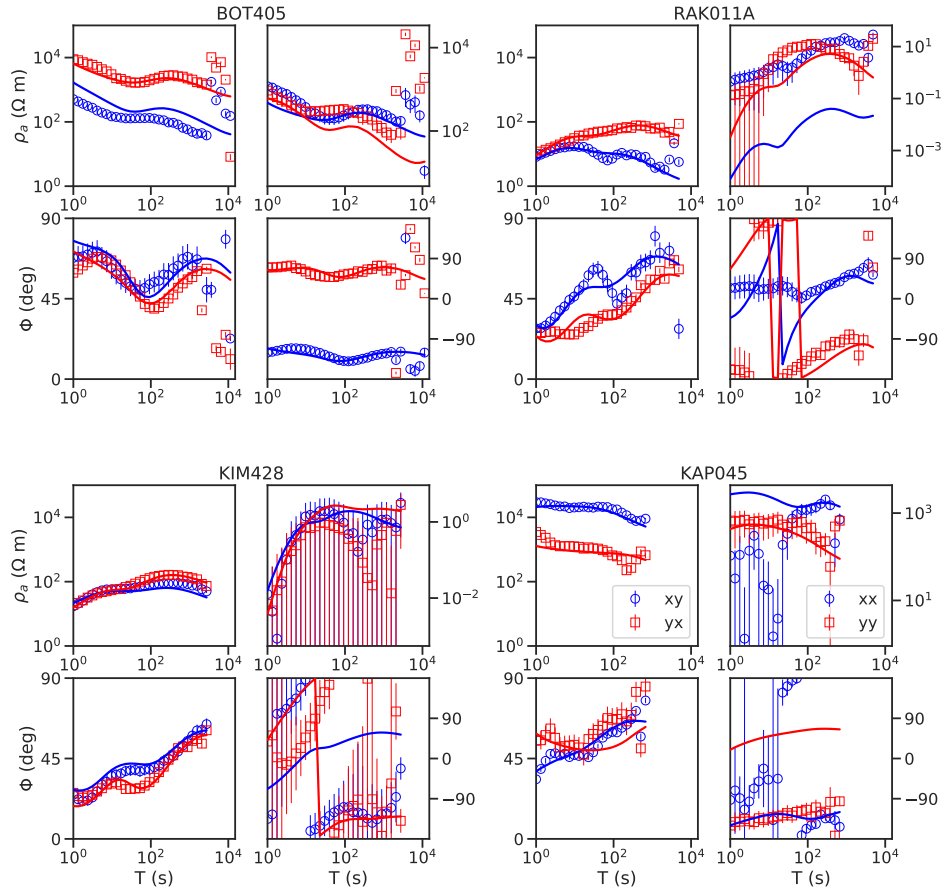


Figure 6. Comparison between observed data (symbols) and predicted data (lines) for the inversion run with *ModEM* and all data for four selected sites marked in Figure 1.

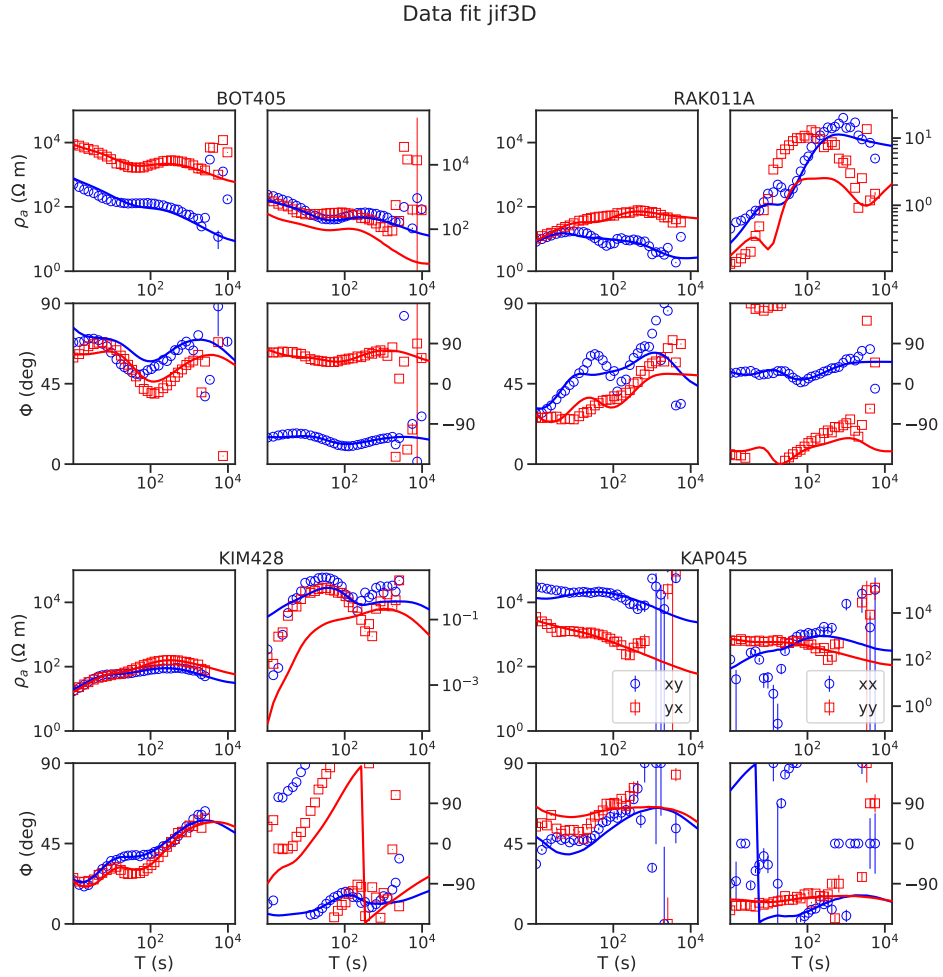


Figure 7. Comparison between observed data (symbols) and predicted data (lines) for the inversion run with *jif3D* and all data for four selected sites marked in Figure 1.

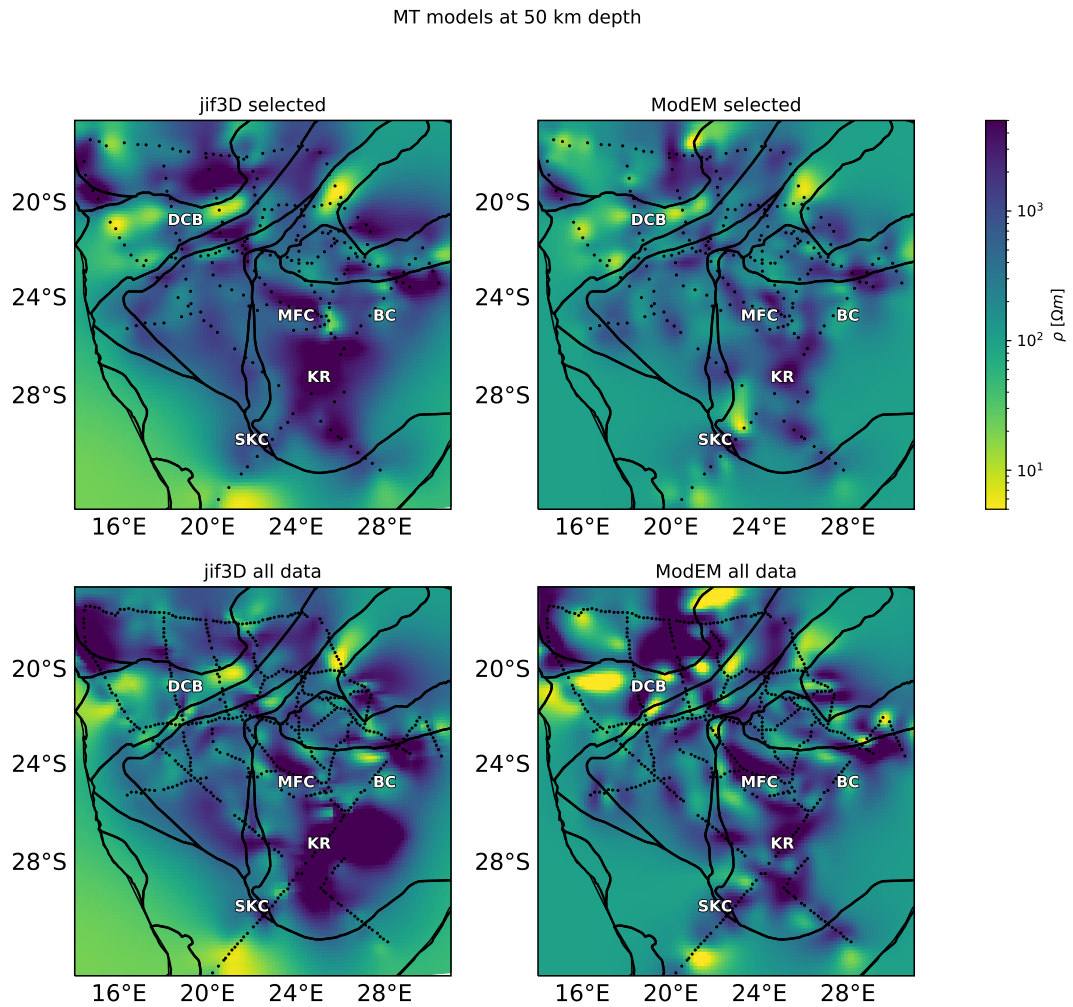


Figure 8. Horizontal slices through the inversion models at a depth of 50 km. We mark several notable structures: Bushveldt Conductor (BC), Damara Conductive Belt (DCB), Kaapvaal Resistor (KR), Molopo Farms Conductor (MFC), Southern Kaapvaal Conductor (SKC).

MT models at 100 km depth

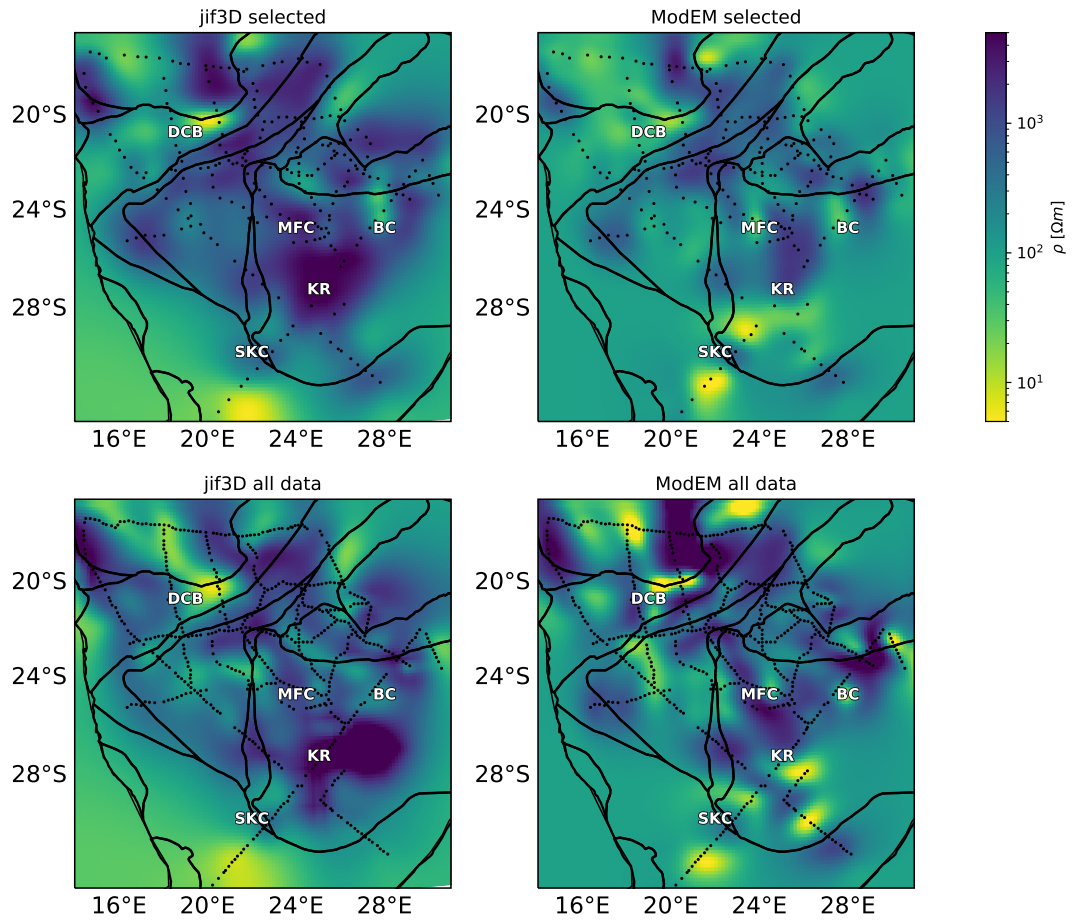


Figure 9. Horizontal slices through the inversion models at a depth of 100 km. For an explanation of abbreviations see Figure 8.

MT models at 150 km depth

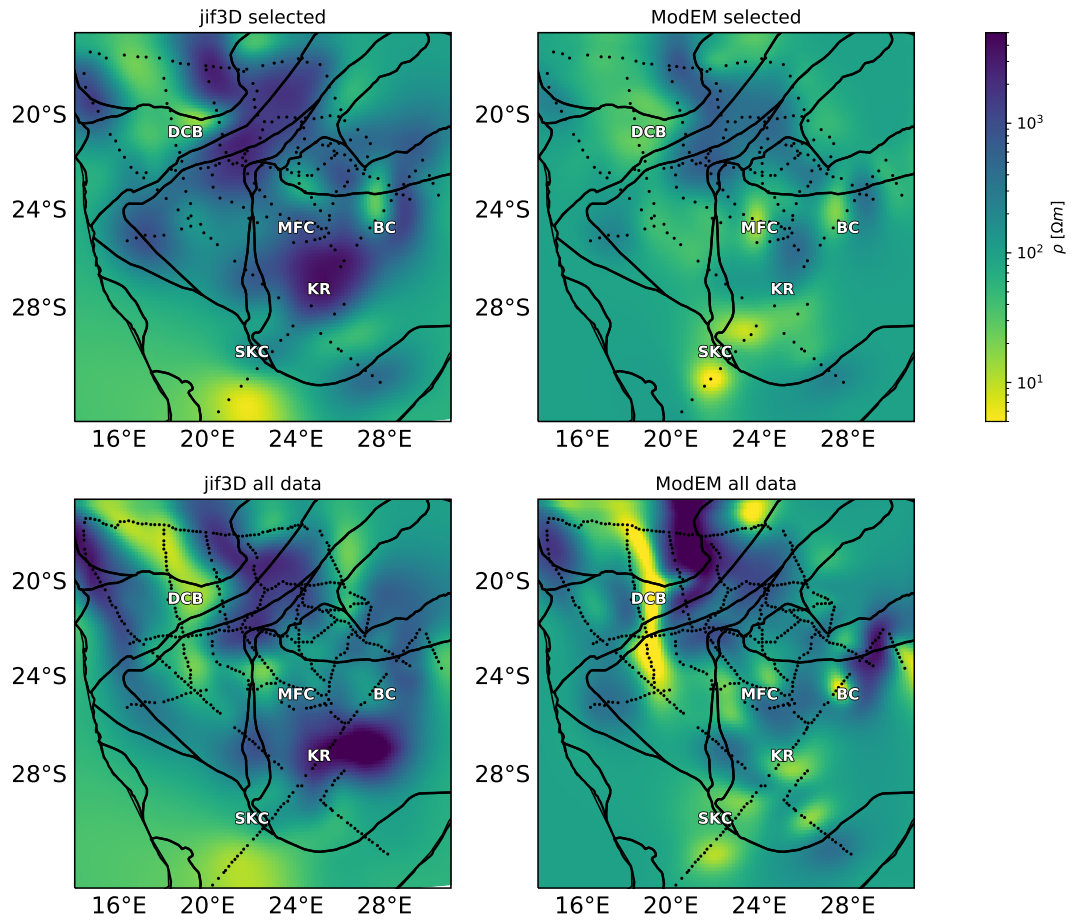


Figure 10. Horizontal slices through the inversion models at a depth of 150 km. For an explanation of abbreviations see Figure 8.

MT models at 200 km depth

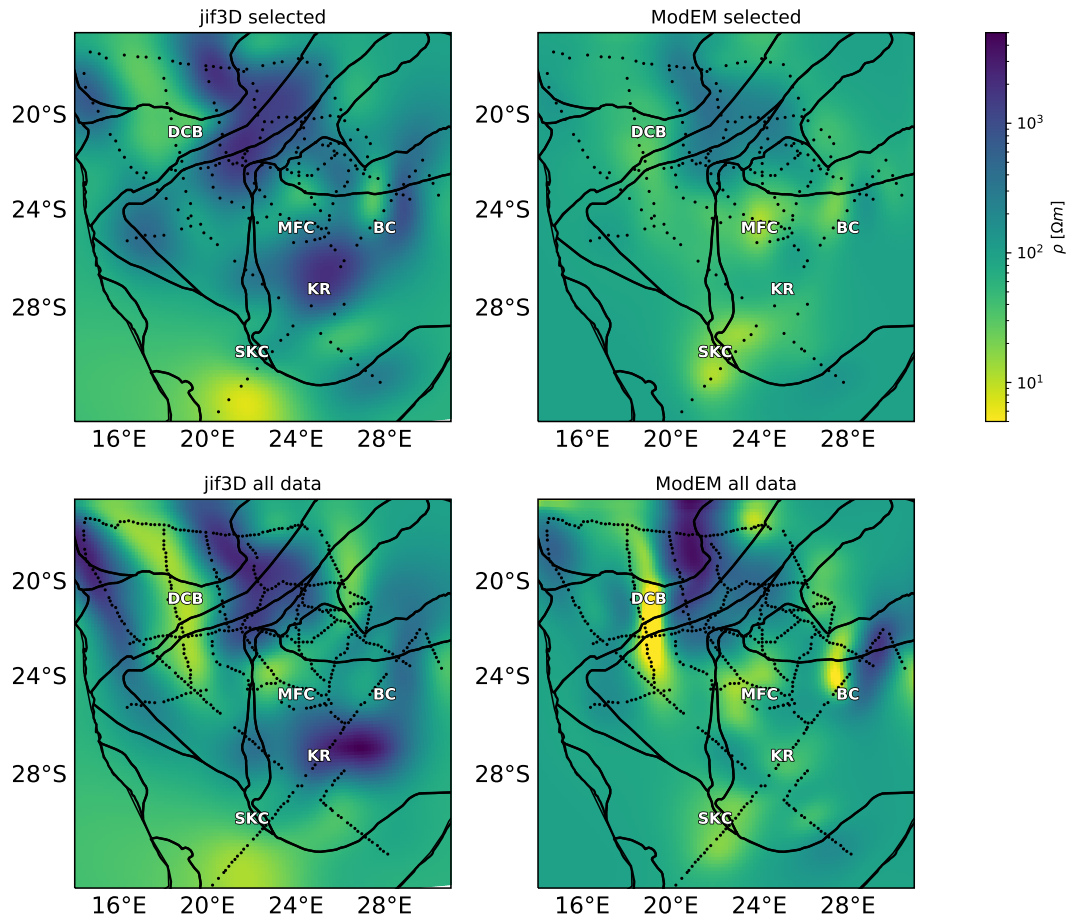


Figure 11. Horizontal slices through the inversion models at a depth of 200 km. For an explanation of abbreviations see Figure 8.

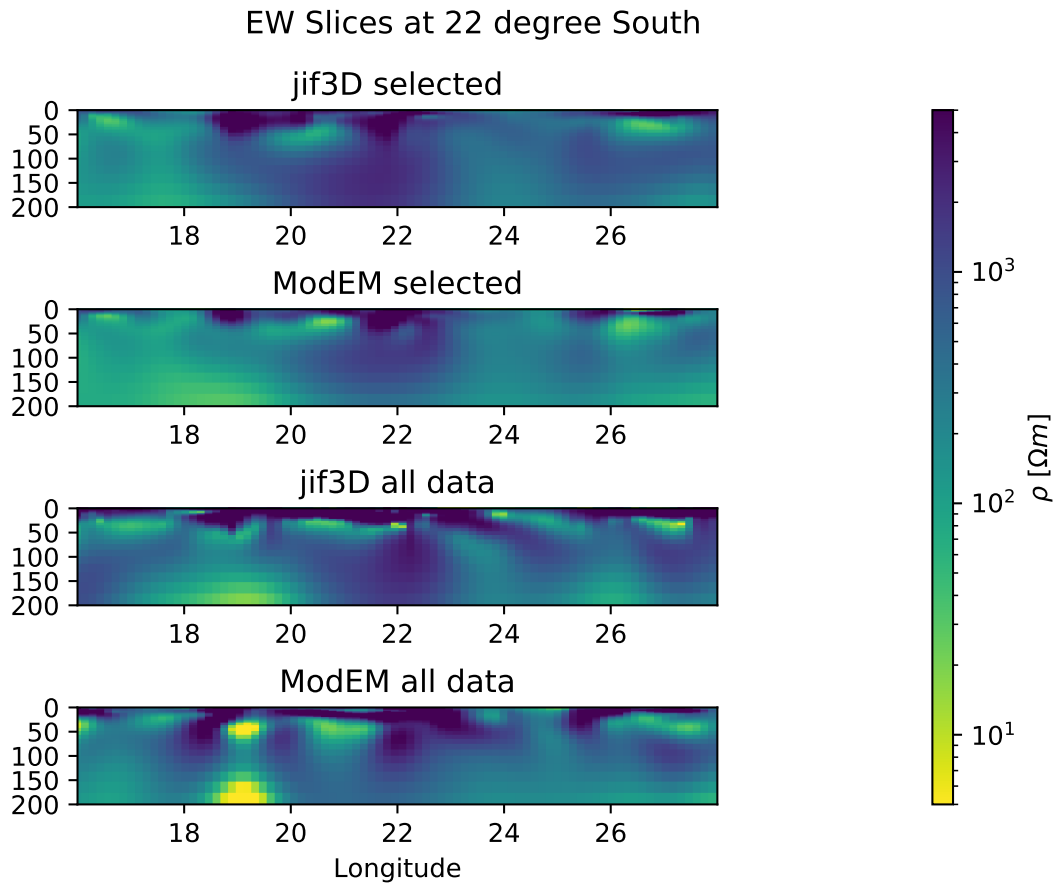


Figure 12. East-west slice through the four inversion models at 22 degree southern latitude (yellow line in Figure 1).

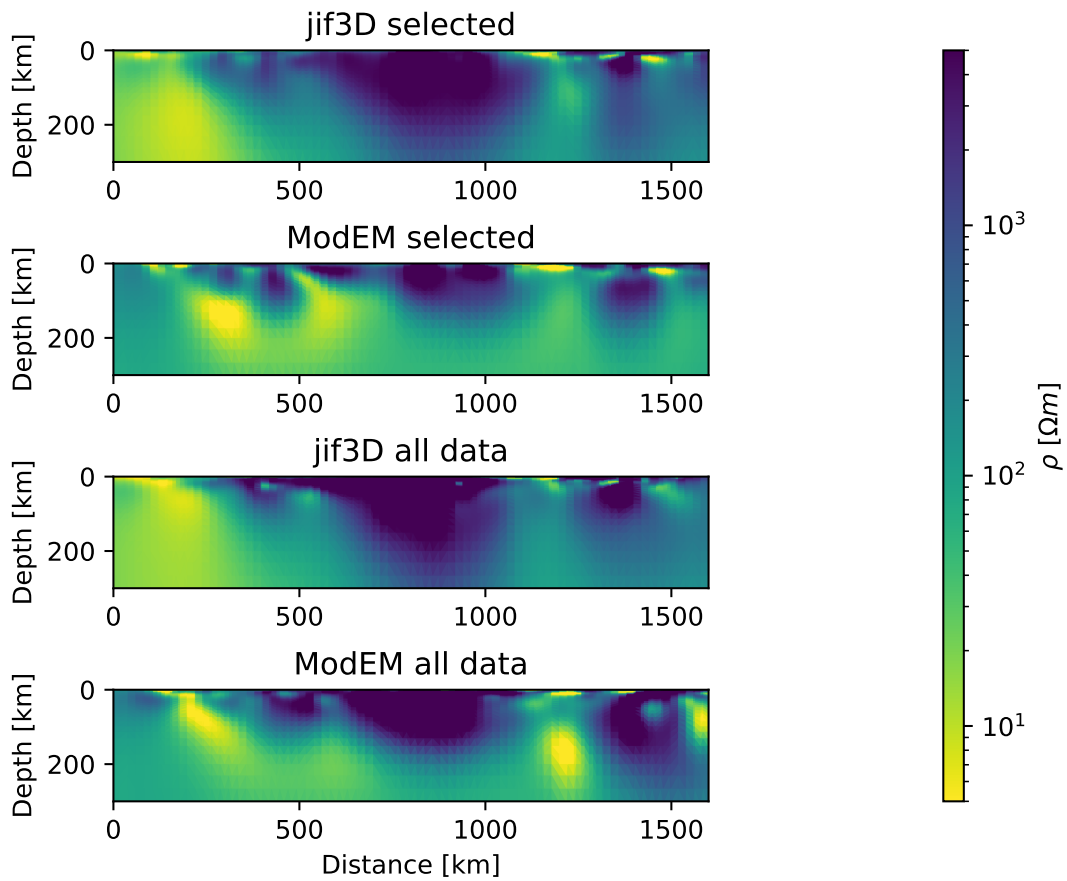


Figure 13. Vertical model slices through the four inversion models along the KAP line (green line in Figure 1). From top to bottom the inversion runs are: *jif3D* with selected data, *ModEM* with selected data, *jif3D* with all data, *ModEM* with all data.

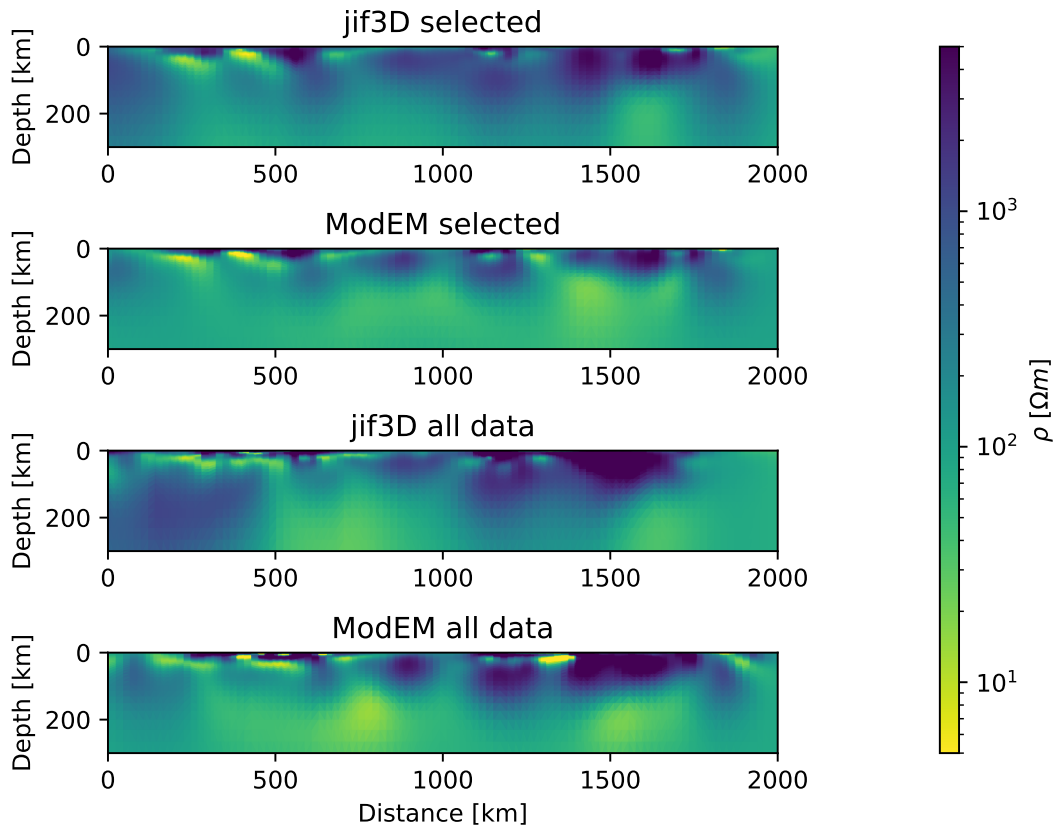


Figure 14. Vertical model slices through the four inversion models along the Kimberley line (red line in Figure 1). From top to bottom the inversion runs are: *jif3D* with selected data, *ModEM* with selected data, *jif3D* with all data, *ModEM* with all data.

Model difference at 50 km depth

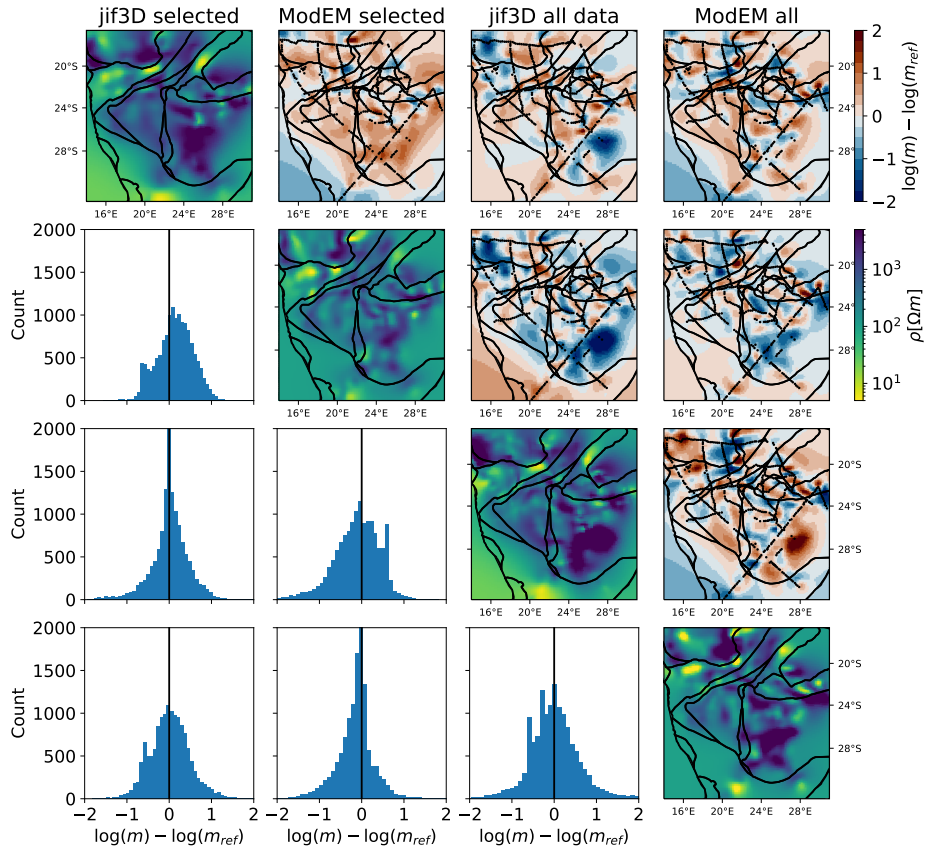


Figure 15. Difference matrix for the four inversion runs at a depth of 50 km. We plot the resistivity slice for each model on the diagonal. Plots above the diagonal show the difference in logarithmic resistivity between pairs of models as labelled above each column, Plots below the diagonal show the corresponding histogram.

Model difference at 150 km depth

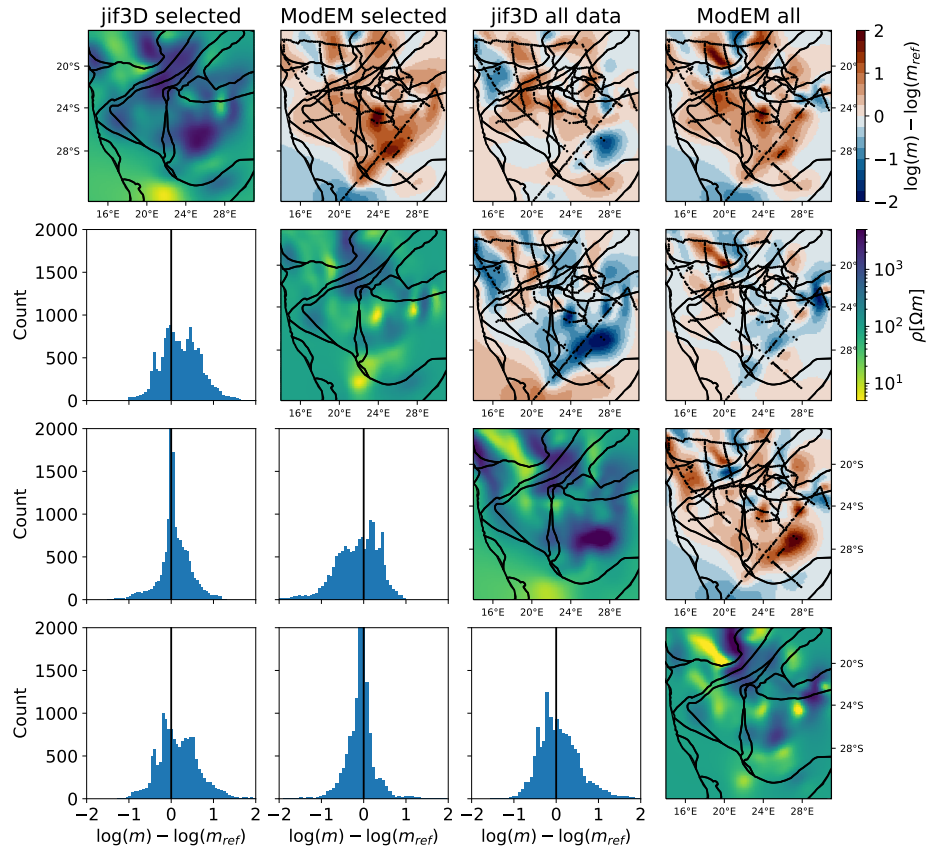


Figure 16. Difference matrix for the four inversion runs at a depth of 150 km. We plot the resistivity slice for each model on the diagonal. Plots above the diagonal show the difference in logarithmic resistivity between pairs of models as labelled above each column, Plots below the diagonal show the corresponding histogram.

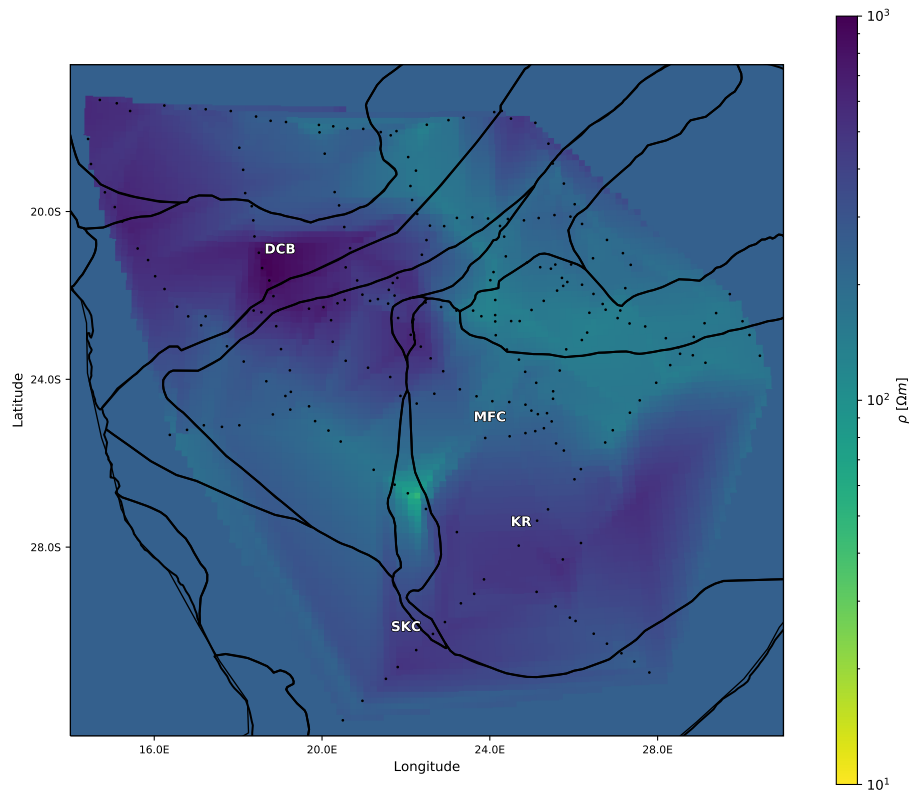


Figure 17. Starting model derived from median apparent resistivity for the inversion with ModEM. Note the reduced range of resistivities in the color bar compared to the other model plots.

Model difference at 50 km depth

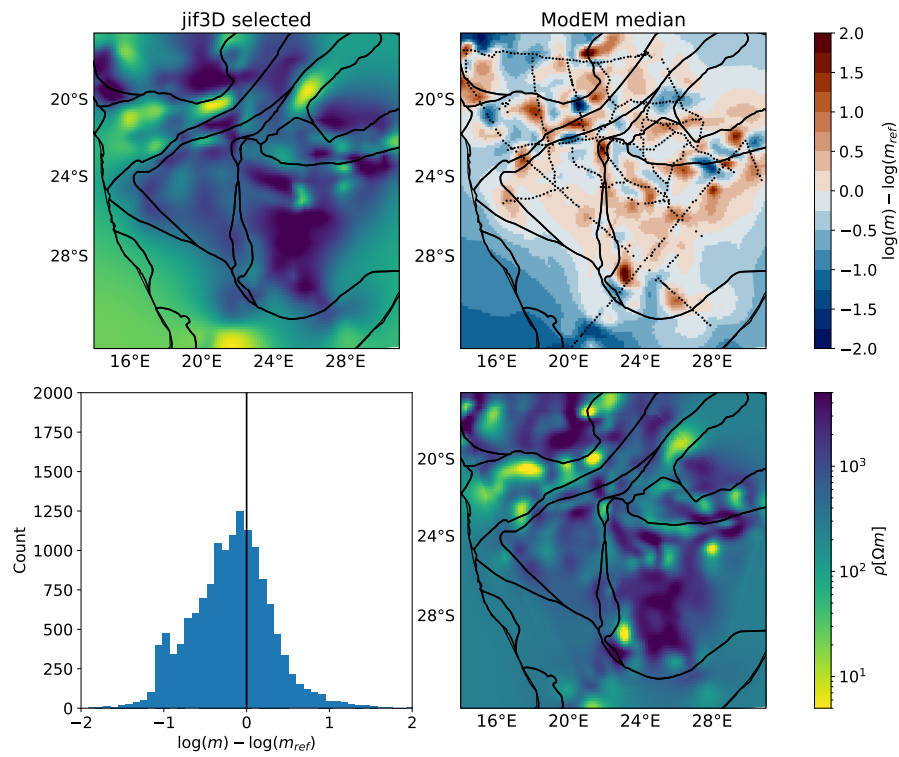


Figure 18. Difference matrix for the ModEM inversion runs with a homogeneous starting model and a median apparent resistivity starting model at a depth of 50 km.

Model difference at 150 km depth

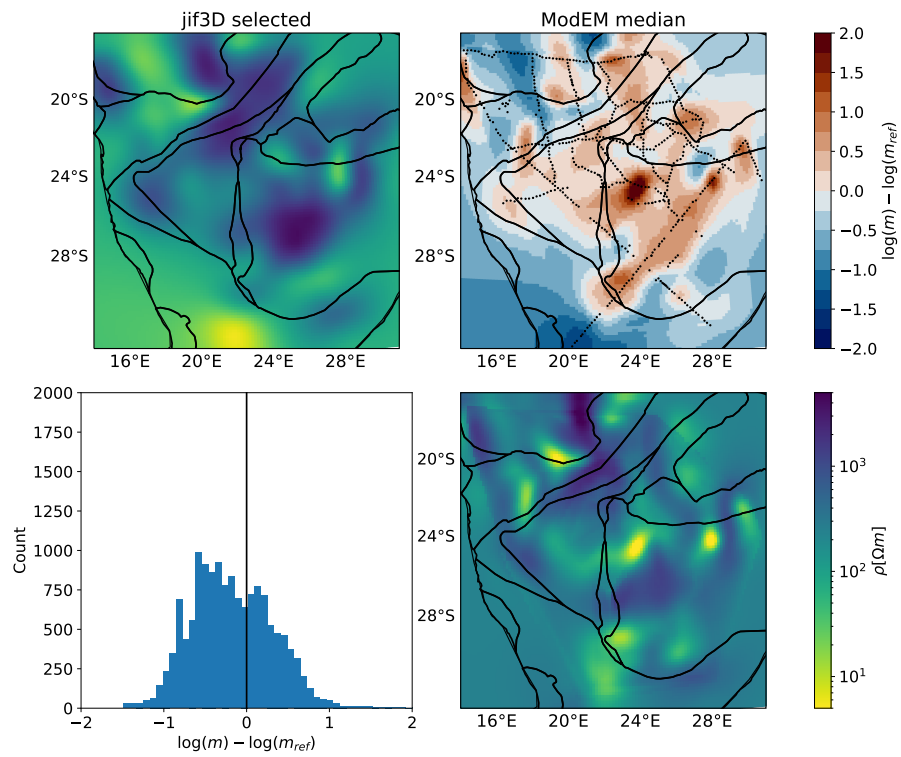


Figure 19. Difference matrix for the ModEM inversion runs with a homogeneous starting model and a median apparent resistivity starting model at a depth of 150 km.

614 **Acknowledgments**

615 MM was funded by the German Research Foundation, DFG, under grant MO 2265/4-
 616 1. SÖ and KS are supported by the Australian Research Council grant FT150100541.
 617 The SAMTEX magnetotelluric impedance estimates used here are available through the
 618 IRIS SPUD repository at <https://doi.org/10.17611/DP/EMTF/SAMTEX>. Download in-
 619 structions for the ModEM inversion software can be found at [https://sites.google](https://sites.google.com/site/modularem/download)
 620 [.com/site/modularem/download](https://sites.google.com/site/modularem/download). jif3D is available via subversion at [https://svn.code](https://svn.code.sf.net/p/jif3d/jif3dsvn/trunk/jif3d)
 621 [.sf.net/p/jif3d/jif3dsvn/trunk/jif3D](https://svn.code.sf.net/p/jif3d/jif3dsvn/trunk/jif3d). Figure 1 was prepared using GMT 6.1 (Wes-
 622 sel et al., 2019), all other Figures with Python. We thank Fabio Cramereri for designing
 623 perceptually uniform color scales used in some of the plots (Cramereri et al., 2020).

624 **References**

- 625 Avdeev, D. B., & Avdeeva, A. (2009). 3d magnetotelluric inversion using a limited-
 626 memory quasi-newton optimization. *Geophysics*, *74*(3), F45-F57. doi: 10.1190/1
 627 .3114023
- 628 Avdeev, D. B., Kuvshinov, A. V., Pankratov, O. V., & Newman, G. A. (1997).
 629 High-performance three-dimensional electromagnetic modeling using modified
 630 Neumann series. Wide-band numerical solution and examples. *Journal of Geomag-*
 631 *netism and Geoelectricity*, *49*, 1519–1539.
- 632 Avdeeva, A., & Avdeev, D. B. (2006). A limited-memory quasi-newton inversion for
 633 1d magnetotellurics. *Geophysics*, *71*(5), G191–G196.
- 634 Avdeeva, A., Moorkamp, M., Avdeev, D. B., Jegen, M., & Miensopust, M. (2015).
 635 Three-dimensional inversion of magnetotelluric impedance tensor data and full
 636 distortion matrix. *Geophysical Journal International*, *202*(1), 464–481.
- 637 Begg, G., Griffin, W., Natapov, L., O’Reilly, S. Y., Grand, S., O’Neill, C., . . . Deen,
 638 T. (2009). The lithospheric architecture of africa: Seismic tomography, mantle
 639 petrology, and tectonic evolution. *Geosphere*, *5*(1), 23–50.
- 640 Beukes, N. J., de Kock, M. O., Vorster, C., Ravhura, L. G., Frei, D., Gumsley, A. P.,
 641 & Harris, C. (2019). The age and country rock provenance of the Molopo farms
 642 complex: Implications for transvaal supergroup correlation in southern Africa.
 643 *South African Journal of Geology*, *122*(1), 39–56. doi: 10.25131/sajg.122.0003
- 644 Campanya, J., Ogaya, X., Jones, A. G., Rath, V., Vozar, J., & Meqbel, N. (2016).
 645 The advantages of complementing mt profiles in 3-d environments with geomag-

- 646 netic transfer function and interstation horizontal magnetic transfer function data:
 647 results from a synthetic case study. *Geophysical Supplements to the Monthly*
 648 *Notices of the Royal Astronomical Society*, 207(3), 1818–1836.
- 649 Celli, N. L., Lebedev, S., Schaeffer, A. J., & Gaina, C. (2020). African cratonic litho-
 650 sphere carved by mantle plumes. *Nature communications*, 11(1), 1–10.
- 651 Chave, A. D., & Jones, A. G. (2012). *The magnetotelluric method*. Cambridge, UK:
 652 Cambridge University press.
- 653 Chave, A. D., & Thomson, D. J. (2003). A bounded influence regression estimator
 654 based on the statistics of the hat matrix. *Journal of the Royal Statistical Society:*
 655 *Series C (Applied Statistics)*, 52, 307–322.
- 656 Clifford, T. N. (1966). Tectono-metallogenic units and metallogenic provinces of
 657 africa. *Earth and Planetary Science Letters*, 1(6), 421–434.
- 658 Crameri, F., Shephard, G. E., & Heron, P. J. (2020). The misuse of colour in science
 659 communication. *Nature communications*, 11(1), 1–10.
- 660 de Ronde, C. E., & de Wit, M. J. (1994). Tectonic history of the barberton green-
 661 stone belt, south africa: 490 million years of archaean crustal evolution. *Tectonics*,
 662 13(4), 983–1005.
- 663 De Wit, M. J., de Ronde, C. E., Tredoux, M., Roering, C., Hart, R. J., Armstrong,
 664 R. A., ... Hart, R. A. (1992). Formation of an archaean continent. *Nature*,
 665 357(6379), 553–562.
- 666 Dong, H., Wei, W., Jin, S., Ye, G., Jones, A. G., Zhang, L., ... Yin, Y. (2020).
 667 Shaping the surface deformation of central and south tibetan plateau: Insights
 668 from magnetotelluric array data. *Journal of Geophysical Research: Solid Earth*,
 669 125(9), e2019JB019206.
- 670 Dong, S.-W., Li, T.-D., Lü, Q.-T., Gao, R., Yang, J.-S., Chen, X.-H., ... Zhou,
 671 Q. (2013). Progress in deep lithospheric exploration of the continental china: A
 672 review of the sinoprobe. *Tectonophysics*, 606, 1–13.
- 673 Egbert, G., & Kelbert, A. (2012). Computational recipes for electromagnetic inverse
 674 problems. *Geophysical Journal International*, 189(1), 251–267.
- 675 Evans, R. L., Jones, A. G., Garcia, X., Muller, M., Hamilton, M., Evans, S., ...
 676 Jelsma, H. (2011). Electrical lithosphere beneath the Kaapvaal craton, southern
 677 Africa. *Journal of Geophysical Research: Solid Earth*, 116(B4).
- 678 Field, M., Stiefenhofer, J., Robey, J., & Kurszlauskis, S. (2008). Kimberlite-hosted

- 679 diamond deposits of southern africa: a review. *Ore Geology Reviews*, *34*(1-2), 33–
680 75.
- 681 Finn, C. A., Bedrosian, P. A., Cole, J. C., Khoza, T. D., & Webb, S. J. (2015).
682 Mapping the 3d extent of the northern lobe of the bushveld layered mafic intru-
683 sion from geophysical data. *Precambrian Research*, *268*, 279–294.
- 684 Fouch, M. J., James, D. E., VanDecar, J. C., Van der Lee, S., & Group, K. S.
685 (2004). Mantle seismic structure beneath the kaapvaal and zimbabwe cratons.
686 *South African Journal of Geology*, *107*(1-2), 33–44.
- 687 Fulla, J., Muller, M., & Jones, A. G. (2011). Electrical conductivity of continental
688 lithospheric mantle from integrated geophysical and petrological modeling: Appli-
689 cation to the Kaapvaal Craton and Rehoboth Terrane, southern Africa. *Journal of*
690 *Geophysical Research: Solid Earth*, *116*(B10).
- 691 Gatzemeier, A., & Moorkamp, M. (2005). 3d modelling of electrical anisotropy from
692 electromagnetic array data: hypothesis testing for different upper mantle conduc-
693 tion mechanisms. *Physics of the Earth and Planetary Interiors*, *149*, 225–242.
- 694 Grégoire, M., Bell, D., & Le Roex, A. (2003). Garnet lherzolites from the kaapvaal
695 craton (south africa): trace element evidence for a metasomatic history. *Journal of*
696 *Petrology*, *44*(4), 629–657.
- 697 Griffin, W., O'Reilly, S., Afonso, J., & Begg, G. (2009). The composition and evolu-
698 tion of lithospheric mantle: A re-evaluation and its tectonic implications. *Journal*
699 *of Petrology*, *50*(7), 1185–1204.
- 700 Griffin, W., O'Reilly, S. Y., Natapov, L., & Ryan, C. (2003). The evolution of litho-
701 spheric mantle beneath the kalahari craton and its margins. *Lithos*, *71*(2-4), 215–
702 241.
- 703 Hamilton, M., Jones, A. G., Evans, R. L., Evans, S., Fourie, C. J. S., Garcia, X., . . .
704 the SAMTEX Team (2006). Electrical anisotropy of South African lithosphere
705 compared with seismic anisotropy from shear-wave splitting analysis. *Physics of*
706 *the Earth and Planetary Interiors*, *158*, 226–239.
- 707 Jones, A. G. (1999). Imaging the continental upper mantle using electromagnetic
708 methods. *Lithos*, *48*(1-4), 57–80.
- 709 Jones, A. G., Evans, R. L., Muller, M. R., Hamilton, M. P., Miensopust, M. P.,
710 Garcia, X., . . . The SAMTEX Team (2009). Area selection for diamonds using
711 magnetotellurics: Examples from southern africa. *Lithos*, *112*, 83–92.

- 712 Jones, A. G., Fishwick, S., Evans, R., Muller, M., & Fullea, J. (2013). Velocity-
 713 conductivity relations for cratonic lithosphere and their application: Example of
 714 Southern Africa. *Geochemistry, Geophysics, Geosystems*, *14*(4), 806–827.
- 715 Jones, A. G., Fullea, J., Evans, R., & Muller, M. (2012). Water in cratonic litho-
 716 sphere: Calibrating laboratory-determined models of electrical conductivity of
 717 mantle minerals using geophysical and petrological observations. *Geochemistry,*
 718 *Geophysics, Geosystems*, *13*(6).
- 719 Karato, S.-i., & Wang, D. (2012). Electrical conductivity of minerals and rocks.
 720 *Physics and Chemistry of the Deep Earth*, 145–236.
- 721 Kelbert, A. (2019). Taking magnetotelluric data out of the drawer. *AGUFM, 2019,*
 722 *IN21A–01.*
- 723 Kelbert, A., & Egbert, G. (2012). Crust and upper mantle electrical conductivity
 724 beneath the Yellowstone Hotspot Track. *Geology*, *40*(5), 447–450.
- 725 Kelbert, A., Meqbel, N., Egbert, G. D., & Tandon, K. (2014). ModEM: A modu-
 726 lar system for inversion of electromagnetic geophysical data. *Computers and Geo-*
 727 *sciences*, *66*, 40–53. doi: 10.1016/j.cageo.2014.01.010
- 728 Kennedy, M. C., & O’Hagan, A. (2001). Bayesian calibration of computer models.
 729 *Journal of the Royal Statistical Society: Series B (Statistical Methodology)*, *63*(3),
 730 425–464.
- 731 Khoza, T. D., Jones, A. G., Muller, M. R., Evans, R. L., Miensopust, M. P., &
 732 Webb, S. J. (2013). Lithospheric structure of an Archean craton and adjacent
 733 mobile belt revealed from 2-D and 3-D inversion of magnetotelluric data: Exam-
 734 ple from southern Congo Craton in northern Namibia. *Journal of Geophysical*
 735 *Research: Solid Earth*, *118*(8), 4378–4397.
- 736 Kirkby, A. L., Musgrave, R. J., Czarnota, K., Doublier, M. P., Duan, J., Cayley,
 737 R. A., & Kyi, D. (2020). Lithospheric architecture of a Phanerozoic orogen from
 738 magnetotellurics: Auslamp in the Tasmanides, Southeast Australia. *Tectonophysics*,
 739 *793*, 228560.
- 740 Kobussen, A. F., Griffin, W. L., & O’Reilly, S. Y. (2009). Cretaceous thermo-
 741 chemical modification of the Kaapvaal cratonic lithosphere, South Africa. *Lithos*,
 742 *112*, 886–895.
- 743 Lee, C.-T. A., Luffi, P., & Chin, E. J. (2011). Building and destroying continental
 744 mantle. *Annual Review of Earth and Planetary Sciences*, *39*, 59–90.

- 745 Mackie, R., Smith, J., & Madden, T. (1994). Three-dimensional electromagnetic
746 modeling using finite difference equations: The magnetotelluric example. *Radio*
747 *Science*, *29*, 923-935.
- 748 McCourt, S., Armstrong, R. A., Jelsma, H., & Mapeo, R. B. (2013). New U-Pb
749 SHRIMP ages from the Lubango region, SW Angola: Insights into the Palaeopro-
750 terozoic evolution of the Angolan Shield, southern Congo Craton, Africa. *Journal*
751 *of the Geological Society*, *170*(2), 353-363. doi: 10.1144/jgs2012-059
- 752 Meqbel, N. M., Egbert, G. D., Wannamaker, P. E., Kelbert, A., & Schultz, A.
753 (2014). Deep electrical resistivity structure of the northwestern US derived from
754 3-d inversion of USArray magnetotelluric data. *Earth and Planetary Science*
755 *Letters*, *402*, 290-304.
- 756 Miensopust, M. P. (2017). Application of 3-d electromagnetic inversion in practice:
757 Challenges, pitfalls and solution approaches. *Surveys in Geophysics*, *38*(5), 869-
758 933.
- 759 Miensopust, M. P., Jones, A. G., Muller, M. R., Garcia, X., & Evans, R. L. (2011).
760 Lithospheric structures and precambrian terrane boundaries in northeastern
761 Botswana revealed through magnetotelluric profiling as part of the Southern
762 African Magnetotelluric Experiment. *Journal of Geophysical Research: Solid*
763 *Earth*, *116*(B2).
- 764 Moorkamp, M., Avdeeva, A., Basokur, A. T., & Erdogan, E. (2020). Inverting
765 magnetotelluric data with distortion correction—stability, uniqueness and trade-off
766 with model structure. *Geophysical Journal International*, *222*(3), 1620-1638. doi:
767 10.1093/gji/ggaa278
- 768 Moorkamp, M., Fishwick, S., Walker, R. J., & Jones, A. G. (2019). Geophysical
769 evidence for crustal and mantle weak zones controlling intra-plate seismicity—the
770 2017 Botswana earthquake sequence. *Earth and Planetary Science Letters*, *506*,
771 175-183.
- 772 Moorkamp, M., Heincke, B., Jegen, M., Roberts, A. W., & Hobbs, R. W. (2011). A
773 framework for 3-D joint inversion of MT, gravity and seismic refraction data. *Geo-*
774 *physical Journal International*, *184*, 477-493. doi: 10.1111/j.1365-246X.2010.04856
775 .x
- 776 Muller, M., Jones, A. G., Evans, R., Grütter, H., Hatton, C., Garcia, X., . . . Ng-
777 wisanyi, T. (2009). Lithospheric structure, evolution and diamond prospectivity

- 778 of the reboth terrane and western kaapvaal craton, southern africa: Constraints
779 from broadband magnetotellurics. *Lithos*, *112*, 93–105.
- 780 Özaydin, S., Selway, K., Griffin, W., & Moorkamp, M. (2021). Composition of the
781 southern african lithospheric mantle and its relevance to magnetotelluric models.
782 *Journal of Geophysical Research*, *submitted*.
- 783 Özaydin, S., & Selway, K. (2020). MATE: An analysis tool for the interpretation of
784 magnetotelluric models of the mantle. *Geochemistry, Geophysics, Geosystems*, 1–
785 26. doi: 10.1029/2020gc009126
- 786 Özaydin, S., Selway, K., & Griffin, W. L. (2021). Are xenoliths from south-
787 western Kaapvaal Craton representative of the broader mantle? Constraints
788 from magnetotelluric modeling. *Geophysical Research Letters*, *48*, 1–11. doi:
789 10.1029/2021GL092570
- 790 Pearce, R., Sánchez de la Muela, A., Moorkamp, M., Hammond, J. O., Mitchell,
791 T., Cembrano, J., ... Pérez Estay, N. (2020). Reactivation of fault systems by
792 compartmentalized hydrothermal fluids in the southern andes revealed by magne-
793 telluric and seismic data. *Tectonics*, e2019TC005997.
- 794 Rao, C., Jones, A. G., Moorkamp, M., & Weckmann, U. (2014). Implications for
795 the lithospheric geometry of the iapetus suture beneath ireland based on electri-
796 cal resistivity models from deep-probing magnetotellurics. *Geophysical Journal*
797 *International*, *198*(2), 737–759.
- 798 Robertson, K., Heinson, G., & Thiel, S. (2016). Lithospheric reworking at the
799 proterozoic–phanerozoic transition of australia imaged using auslamp magnetotel-
800 luric data. *Earth and Planetary Science Letters*, *452*, 27–35.
- 801 Robertson, K., Thiel, S., & Meqbel, N. (2020). Quality over quantity: On work-
802 flow and model space exploration of 3d inversion of MT data. *Earth, Planets and*
803 *Space*, *72*(1), 1–22.
- 804 Selway, K. (2014). On the causes of electrical conductivity anomalies in tectonically
805 stable lithosphere. *Surveys in Geophysics*, *35*(1), 219–257.
- 806 Selway, K. (2018). Electrical discontinuities in the continental lithosphere imaged
807 with magnetotellurics. *Lithospheric discontinuities*, 89–109.
- 808 Selway, K., Ford, H., & Kelemen, P. (2015). The seismic mid-lithosphere discontinu-
809 ity. *Earth and Planetary Science Letters*, *414*, 45–57.
- 810 Sodoudi, F., Yuan, X., Kind, R., Lebedev, S., Adam, J. M.-C., Kästle, E., &

- 811 Tilmann, F. (2013). Seismic evidence for stratification in composition and
812 anisotropic fabric within the thick lithosphere of kalahari craton. *Geochemistry,*
813 *Geophysics, Geosystems*, 14(12), 5393–5412.
- 814 Thiel, S., Goleby, B. R., Pawley, M. J., & Heinson, G. (2020). Auslamp 3d mt imag-
815 ing of an intracontinental deformation zone, musgrave province, central australia.
816 *Earth, Planets and Space*, 72(1), 1–21.
- 817 VanTongeren, J. A. (2018). Mixing and unmixing in the bushveld complex magma
818 chamber. *Processes and Ore Deposits of Ultramafic-Mafic Magmas through Space*
819 *and Time*, 113–138.
- 820 Wannamaker, P., Hill, G., Stodt, J., Maris, V., Ogawa, Y., Selway, K., . . . Ayling,
821 B. (2017). Uplift of the central transantarctic mountains. *Nature communications*,
822 8(1), 1–11.
- 823 Wessel, P., Luis, J., Uieda, L., Scharroo, R., Wobbe, F., Smith, W., & Tian, D.
824 (2019). The generic mapping tools version 6. *Geochemistry, Geophysics, Geosys-*
825 *tems*, 20(11), 5556–5564.
- 826 White-Gaynor, A., Nyblade, A., Durrheim, R., Raveloson, R., van der Meijde, M.,
827 Fadel, I., . . . Titus, N. (2020). Lithospheric boundaries and upper mantle struc-
828 ture beneath southern africa imaged by p and s wave velocity models. *Geochem-*
829 *istry, Geophysics, Geosystems*, 21(10), e2020GC008925.